Ions Adsorbed at Amorphous Solid / Solution Interfaces Form Wigner Crystal-Like Structures

Jianan Wang,[1] Hua Li,[1,2] Mahdi Tavakol,[3] Alessandra Serva,[4] Brett Nener,[5] Giacinta Parish,[5] Mathieu Salanne,[4] Gregory G. Warr,[6] Kislon Voïtchovsky,[5] Rob Atkin[1*]

[1]School of Molecular Sciences, The University of Western Australia, Perth, 6009, Australia

[2]Centre for Microscopy, Characterisation and Analysis, The University of Western Australia, Perth, 6009, Australia

[3]Department of Physics, Durham University, Durham, DH1 3LE, UK

[4]Sorbonne Université, CNRS, Physicochimie des Électrolytes et Nanosystèmes Interfaciaux, PHENIX, Paris, F-75005, France

[5]School of Engineering, The University of Western Australia, Perth, 6009, Australia

[6]School of Chemistry and Sydney Nano Institute, The University of Sydney, Sydney, 2006, Australia

*E-mail: rob.atkin@uwa.edu.au

19 **TOC Graphic**

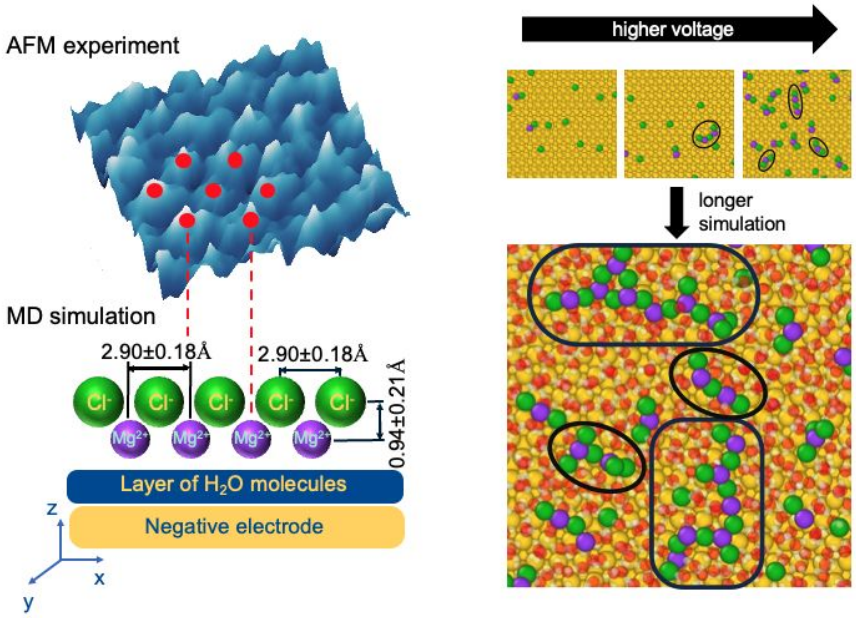

20

21

Abstract

When a surface is immersed in a solution, it usually acquires a charge, which attracts counterions and repels co-ions to form an electrical double layer. The ions directly adsorbed to the surface are referred to as the Stern layer. The structure of the Stern layer normal to the interface was described decades ago, but the lateral organization within the Stern layer has received scant attention. This is because instrumental limitations have prevented visualization of the ion arrangements, except for atypical, model, crystalline surfaces. Here, we use high resolution amplitude modulated atomic force microscopy images to visualize *in situ* the lateral structure of Stern layer ions adsorbed to polycrystalline gold, and amorphous silica and gallium nitride (GaN). For all three substrates, when the density of ions in the layer exceeds a system-dependent threshold, correlation effects induce the formation of close packed structures akin to Wigner crystals. Depending on the surface and the ions, the Wigner crystal-like structure can be hexagonally close packed, cubic, or worm-like. The influence of electrolyte concentration, species, and valence, as well as the surface type and charge, on the Stern layer structures is described. When the system parameters are changed to reduce the Stern layer ion surface excess below the threshold value, Wigner crystal-like structures do not form, and the Stern layer is unstructured. For gold surfaces, molecular dynamic simulations reveal that when sufficient potential is applied to the surface ion clusters form with dimensions similar to the Wigner crystal-like structures in the AFM images. The lateral Stern layer structures presented, and in particular the Wigner crystal-like structures, will influence diverse applications in chemistry, energy storage, environmental science, nanotechnology, biology, and medicine.

Keywords: Stern layer, solid/liquid interface, electrical double layer, AFM, electrolyte

Introduction

Surfaces in water usually become charged[1]. The surface charge may be acquired *via* the protonation/deprotonation of surface groups, ion adsorption to or desorption from the surface, ion exchange between the surface and the solution, or application of an external potential to an electrode[1,2]. In 1853, Helmholtz recognized that charged electrodes immersed in electrolytes attract counterions and repel co-ions[3], and in the 1910s, the Gouy–Chapman model introduced the concept of a diffuse ion layer[4,5]. In 1924, Stern combined and advanced these theories *via* the Gouy-Chapman-Stern (GCS) model of the electrical double layer (EDL)[6], which consists of a surface-bound Stern layer and a near-surface diffuse layer. The final major insight came in 1947, when Grahame defined dehydrated ions in direct contact with an electrode as specifically adsorbed[7], with their center defining the so-called inner Helmholtz plane (IHP), parallel to the surface. By extension the outer Helmholtz plane (OHP) is defined by the centers of solvated ions adsorbed to the electrode. However, this model of the EDL only describes the ion density profile normal to the interface, implicitly assuming an averaged picture in any plane parallel to the surface, including the Stern layer. The view is well accepted for dilute solutions, and has been studied at diverse interfaces ranging from metals[8], mineral oxides[9] (such as silica, alumina, titania), clays[10] and refractories like mica[11], to hydrophobic solids like graphite[12] and Teflon[13], as well as soft interfaces including oil droplets[14], proteins[15], self-assembled surfactant[16] and lipid aggregates[17], and bubbles[18].

Aside from advances regarding the properties of near-surface solvent and permittivity[19], our understanding of the structure of the Stern layer has hardly progressed over the last 75 years, yet critical questions are outstanding[2]. The lateral arrangement of Stern layer ions across the surface remains elusive. Apart from the specific case of crystalline substrates which strongly

template ion adsorption,[20–26] it is generally assumed that ions adsorb onto irregularly spaced surface charge sites of amorphous substrates, resulting in a laterally disordered Stern layer.[27] As a result, the impact of the lateral Stern layer structure on the interfacial properties remains largely unexplored. Another puzzle is overcharging (also known as charge inversion or charge reversal), where more counterions adsorb in the Stern layer than are required for surface charge neutralization. Overcharging has been known since at least the 1960s when multivalent ions were found to overcharge clay, latex, and mineral oxide surfaces[28–31], and recently, monovalent ions have been found to reverse the surface charge of titania and mica at high concentrations[32–36]. Classical GCS mean-field theory cannot account for overcharging[2,37–39], and two competing theories have emerged, referred to as the "chemical" and "physical" models. The "chemical" model argues that overcharging is caused by specific ion adsorption driven by non-Coulombic forces, such as chemical bonds, hydrogen bonds, complex formation and hydrophobic interactions[2,37–40]. On the other hand, the "physical" model argues that ion-ion correlations are key, and that specific ion sizes and interactions must be considered, such as excluded volume and hard-core effects[37]. A consequence of this second model is that when a threshold electrolyte concentration is exceeded, the magnitude of lateral repulsions between Stern layer counterions is greater than surface – counterion attractions. When this occurs, it is proposed that the counterions order into a hexagonally close packed (HCP) Wigner crystal-like structure to minimize repulsions, and co-ions adsorb to the Stern layer to partially neutralize the excess charge[40]. While the chemical approach has received some, though not conclusive, experimental validation[32,33,41,42], the physical theory is controversial, and Wigner crystal-like Stern layer structures have not been observed experimentally[37]. Recent instrumental advances mean that it is now possible to study the lateral structure of Stern layers on amorphous surfaces to probe whether Wigner crystal-like structures form, and therefore discriminate between overcharging mechanisms.

Before now, lateral Stern layer structures of aqueous electrolytes have only been visualized using atomic force microscopy (AFM) on atomically smooth, crystalline surfaces such as mica[20–26,43,44], calcite[22] and gibbsite[45]. On these surfaces, the charge site lattice of the underlying substrate templates crystalline Stern layers: HCP on mica and gibbsite, and rhombic on calcite. These well-defined repeating structures are ideal for AFM imaging, motivating the focus on these crystalline surfaces in the first place. However, these Stern layers are not Wigner crystal-like structures because ion arrangements are primarily determined by the epitaxial effect of the surface lattice rather than lateral ion correlations. In any case, the wide applicability of results for these crystalline surfaces is limited[46] because the vast majority of surfaces are not crystalline, but amorphous. This is true whether in the context of advanced materials (surfaces) research and technology, or in living systems.

Here, lateral Stern layer structures were investigated on three representative surfaces: poly-crystalline gold, amorphous silica, and gallium nitride (GaN) with an amorphous oxide surface. Gold was studied because it is an exemplar metal electrode, silica as one of the most common and widely studied surfaces[47], and GaN for its applications in sensing and catalysis[48,49]. We show that Stern layer ions form ordered, Wigner crystal-like structures on amorphous surfaces consistent with the "physical" overcharging model, even at low-to-moderate (including biologically relevant[50]) electrolyte concentrations once the ion adsorption density exceeds a minimum threshold value.

Results and Discussion

In this work, Stern layers were imaged using amplitude modulated atomic force microscopy (AM-AFM). In AM-AFM experiments, the AFM tip and the surface are completely immersed in the solution, and the AFM cantilever is oscillated near its resonance frequency[51]. Away from the surface, the cantilever oscillates at a free amplitude (A_0), a parameter that can be adjusted externally. As the tip approaches the surface, the vibration is damped to a reduced amplitude $A < A_0$. During imaging, the oscillation amplitude is maintained at a working amplitude, A_S below A_0 by the AFM feedback control, which constantly adjusts the tip – surface distance[52]. These readjustments provide a picture of the surface topography. The phase shift of the cantilever oscillation, acquired simultaneously with the topography, can vary freely and is sensitive to the compliance of the material between the tip and the surface (conservative vs. dissipative interactions). Phase images are known to be often more effective in mapping the position and hydration status of ions in interfacial systems[23]. Here we found the phase information particularly effective for imaging anion-rich Stern layers obtained for positive surface potentials. The topography and phase images, presented in the Supporting Information (SI), are in excellent agreement, and the features scale correctly, eliminating the possibility of imaging artifacts.

Gold

Fig. 1 compares AM-AFM phase images of gold surfaces in deionized (DI) water at open circuit potential (OCP) (Fig. 1a) with 0.35 M $MgCl_2$ at OCP – 0.3 V (Fig. 1b–d). The image of the gold surface in water (Fig. 1a) shows rows of bright spots, which the two-dimensional fast-Fourier transform (2D-FFT) image (inset) shows to be 5.5 Å apart on average with a diffuse background indicating undulation. The root-mean-square (RMS) roughness of the gold surface is 25 pm over the 10 nm × 10 nm area (Fig. S6). These results are consistent with a

polycrystalline gold surface formed by reconstruction of the surface gold atoms, producing structural defects[53,54].

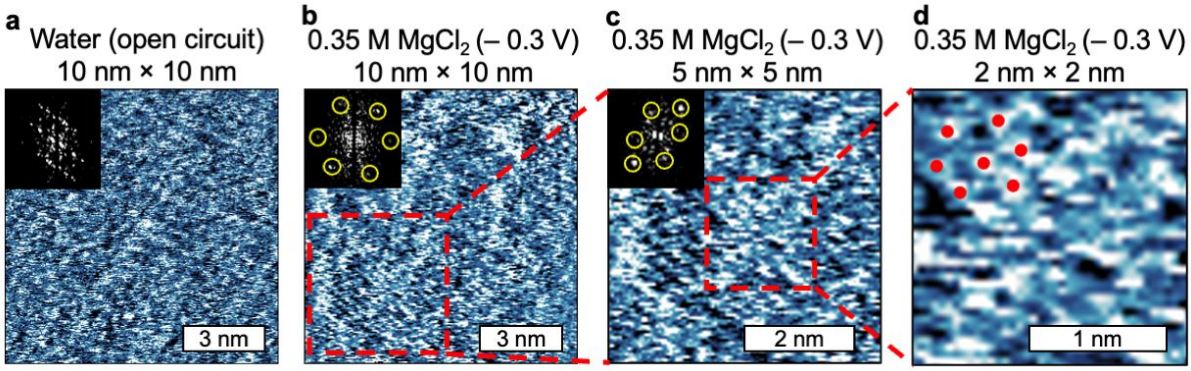

Fig. 1. AFM phase images of the solid/liquid interfaces of gold. The images are taken first in deionized (DI) water at open circuit potential (OCP) (a). Then, the images are taken in 0.35 M $MgCl_2$ at –0.3V vs. the open circuit potential (b–d). The 10 nm × 10 nm image (b) is enlarged to 5 nm × 5 nm (c, corresponding to the dashed square in (b)) and 2 nm × 2 nm (d, corresponding to the dashed squares in (c)). Insets: two-dimensional fast-Fourier transforms (2D-FFT) of the corresponding images; yellow circles in the FFT images highlight the bright spots showing repetitive patterns of the Stern layers. Red dots in the 2 nm × 2 nm images show features aligned in a hexagonally close packed structure.

The image in the presence of the electrolyte (Fig. 1b–d) is starkly different. Most notably, the average spacing between features is 2.8 Å from the FFT, close to half the distance for the polycrystalline gold in water (Fig. 1a), so the image does not represent features of the substrate. In AM-AFM phase images, adsorbed ions may appear as either a bright[55,56] or dark spot[23] depending on the surface and imaging conditions. Comparison of the phase images in Fig. 1 with their corresponding topography images (Figs. S5 and S9) reveals that the bright phase spots coincide with topographical protrusions and are hence interpreted as individual adsorbed Stern layer ions.

Stern layer ions on the gold surface in 0.35 M $MgCl_2$ at OCP – 0.3 V (Fig. 1b) are organized into rows of small oval features that become more obvious as the magnification is increased (Fig. 1c, d). At the lowest resolution (10 nm × 10 nm), the dominant row direction is diagonal in the lower left of the image (i.e. within the red square), but vertical in the top right. As the electric field is uniform across the surface, this means the rows are not due to ions aligning in the field direction.

The significant negative surface potential dictates that cations are enriched and more confined in the Stern layer due to electrostatic adsorption, so the imaged features are most likely to be Mg^{2+} ions. Hydrated Mg^{2+} ions are 8.6 Å in diameter[57], whilst dehydrated Mg^{2+} ions are 1.7 Å in diameter[58]. The size of individual features in Fig. 1 is 2.2 ± 0.4 Å (determined by measuring 15 randomly chosen features in two directions each) and the spacing between features of 2.8 Å (FFT image in Fig. 1b) which suggest that Mg^{2+} ions in the Stern layer are partially or fully dehydrated. These structures shown in Fig. 1 were consistent when imaged with both silica and diamond AFM tips (Figs. S9 and S10), so do not depend on AFM tip surface chemistry. The 5 nm × 5 nm (Fig. 1c) and 2 nm × 2 nm (Fig. 1d) zoomed-in regions confirm the rows of oval features, but in the 2 nm × 2 nm image, red dots have been placed approximately in the center of 7 features to highlight the hexagonally close packed (HCP) arrangement of the Stern layer ions.

This highly structured, HCP ion arrangement is consistent with Wigner crystal-like Stern layer structures[40] for 0.35 M $MgCl_2$ at – 0.3 V on gold. The presence of HCP Wigner crystal-like structures means that the ion-ion correlations of the "physical" model must operate in the Stern layer[40]. The observation of at least partial dehydration of Stern layer ions means that specific ion adsorption may contribute to interactions with the substrate, but do not determine the

location or lateral arrangement in the Stern layer; specific adsorption cannot explain the Wigner crystal-like Stern layer structures on non-crystalline surfaces, so the ion correlations of the "physical" model must dominate "chemical" effects. A hydration network within and immediately above the Stern layer could also contribute to lateral order in Stern layers,[23] but we are unable to image or otherwise detect water individual molecules.

Fig. 1 shows that there are ~ 9 ions / nm^2 for the gold electrode at –0.3 V immersed in an 0.35 M $MgCl_2$ solution. This is equivalent to a Stern layer charge density of ~18 charges/nm^2 assuming Mg^{2+} adsorption. The "physical" model states that Wigner crystal-like structures can form at high ion concentrations when electrostatic coupling parameter, $\Xi = 2\pi\sigma l_B^2 z^3/e$, is greater than 10[2,59], where σ, l_B, z and e are surface charge density, Bjerrum length $l_B = e^2/(4\pi\varepsilon_r\varepsilon_0 k_B T)$, ion valency and elementary charge, respectively. At 25 ºC in dilute aqueous solution (ε_r = 78), Ξ = 10 corresponds to a Stern layer charge density of 3.1 charges/nm^2 in a monovalent salt, but to only ~0.4 charges/nm^2 for a divalent counterion. This means the observed Stern layer charge density of ~ 18 charges/nm^2 in 0.35 M $MgCl_2$ far exceeds the threshold Stern layer charge density for ion correlations, in accordance with observation of Wigner crystal-like structures.

Wigner crystal-like structures form when the Stern layer ion surface excess is sufficiently high to induce lateral ion – ion correlations. Conversely, when the density of Stern layer ions is below that threshold, ions are expected to be disordered. In addition, the structure of the adsorbed water layer and ionic species may change upon the extent of the electronic screening inside the substrate material (as measured by its dielectric constant or by a screening length in the framework of the Thomas-Fermi model)[60–62] as well as the applied voltage in the case of metallic electrodes, leading to a competition between ions and water molecules to populate the

first adsorbed layer.[63] By manipulating the system conditions (bulk electrolyte concentration and surface potential) to decrease the density of Stern layer ions until amorphous layers were observed, the system-dependent threshold conditions for Wigner crystal-like structures could be approximately determined. Fig. 2 presents the AFM images of Stern layers of a gold surface immersed in $MgCl_2$ solutions of various concentrations (0.1 M, 0.2 M, 0.35 M) and surface potentials (– 0.3 V, – 0.2 V, 0 V, + 0.2 V, + 0.3 V, all relative to OCP) together with schematic representations of the ionic species in the Stern layer. The image presented for – 0.3 V is from a different experiment to the data presented in Fig. 1 which gives an indication of the variability in the Wigner crystal-like structures between experiments.

At – 0.3 V in 0.35 M $MgCl_2$, the adsorbed ions form a Wigner crystal-like structure (Fig. 2c), but reducing the concentration from to 0.2 M (Fig. 2b), decreases the crystallinity of the Stern layer: rows form in sections of the image, but the Stern layer is less well structured, confirmed by the vertical bands in the inset FFT. Further decreasing concentration to 0.1 M (Fig. 2a) causes fewer ions adsorb, but the image remains different to that of the gold surface in DI water, confirming that ions still adsorb. The random arrangement of the ions is consistent with an amorphous Stern layer, as is the diffuse FFT image. Here the apparent larger image feature size is consistent with a reduced surface excess consistent with more thermally mobile ions. Under this condition, it is also unlikely that the Stern layer Mg^{2+} ions overscreen the surface charge. This means that for adsorbed Mg^{2+} ions on polycrystalline gold at – 0.3 V, the threshold concentration for the formation of Wigner crystal-like structures is between 0.2 M and 0.35 M.

The effect of surface potential is similar. When the potential in 0.35 M $MgCl_2$ is decreased from – 0.3 V to – 0.2 V (Fig. 2d), the crystallinity is again disrupted. In the top-right corner of Fig. 2d the ions remain in straight rows, but in the bottom-right corner rows are curved,

indicating weaker ion correlations consistent with Wigner glass-like structures[64–66]. As a result, in the FFT image, only one pair of bright spots corresponding to the near-horizontal rows are retained. At OCP (Fig. 2e), attraction of ions to the surface is weak, resulting in an even lower Mg^{2+} surface excess and a disordered Stern layer, also confirmed by the diffuse FFT image. Here again the apparent size of each Stern layer ion is much larger than in the Wigner crystal-like structure. This means that the threshold surface potential for a Wigner crystal-like structure to form on polycrystalline gold lies between – 0.2 V and – 0.3 V (vs. OCP) at a $MgCl_2$ concentration of 0.35 M.

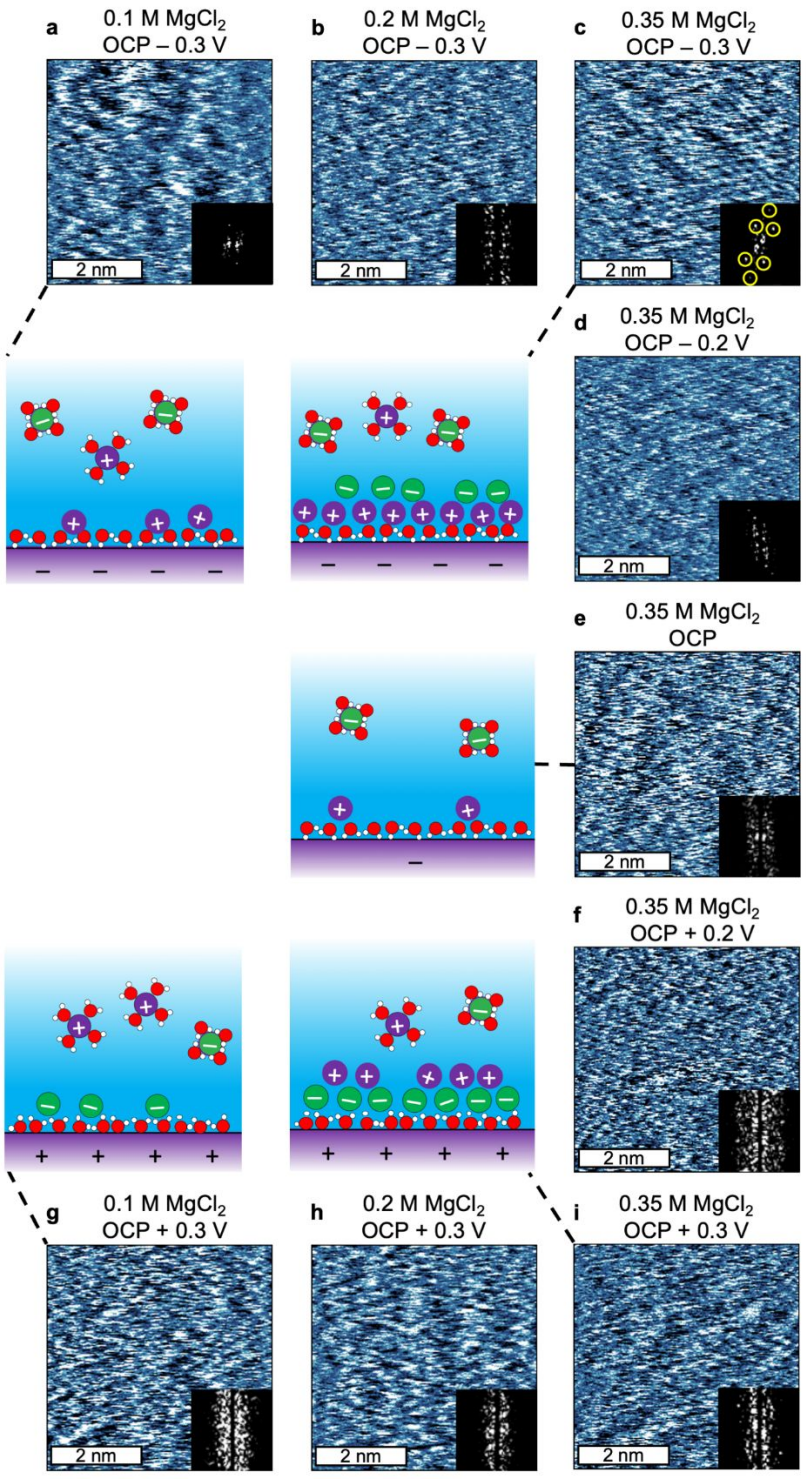

Fig. 2. 5 nm × 5 nm AFM phase images of the interfaces between a gold surface and $MgCl_2$ solutions at various concentrations and surface potentials as labelled. The DI water was saturated with CO_2 and has a pH of ~ 5.5. No acids or bases were added to the $MgCl_2$ solutions to adjust the solution pH. OCP: open circuit potential. Insets: 2D-FFT of the corresponding images. Also shown are simplistic schematic representations of the ionic species in the Stern layers and near-surface layers for the corresponding AFM images as indicated by connecting dashed lines.

Similar trends were found when a positive bias was applied to the gold surface in $MgCl_2$ solutions. When the gold surface is positively polarized, the Stern layer consists of adsorbed Cl^- ions which are most likely the species imaged in Fig. 2f–i. Fig. 2f shows that for 0.35 M $MgCl_2$ at + 0.2 V, the adsorbed ions form rows in the bottom-left and the top-left of the images, but the imaged layer appears amorphous in other area. The FFT image shows two pairs of bright spots on a strong background, so crystallinity is weak. However, when the potential is increased to + 0.3V (Fig. 2i), the ions align in rows in a large area near the center of the image, consistent with weakly formed Wigner crystal-like structures. Higher potentials could not be investigated due to electrochemical breakdown of water. The image is less clear than when Mg^{2+} ions adsorb at – 0.3 V, and there is only one pair of bright spots in the FFT. This reduced clarity for the features in the images at positive potentials is not due to instrumental or experimental limitations, as it could be consistently reproduced. Rather, it is attributed to a stronger attraction between the divalent Mg^{2+} ions and the gold surface when compared to monovalent Cl^- ions at similar (but opposite sign) potentials. Consequently, compared to Mg^{2+}, the Cl^- surface excess, and therefore ion correlations, are reduced, even at twice the ion concentration.

For Cl^- Stern layers, crystallinity decreases markedly when the electrolyte concentration is decreased at + 0.3 V. For 0.2 M at + 0.3 V (Fig. 2h), there are multiple row directions, and the feature size is large, consistent with weaker ion – ion correlations. These effects are more pronounced when the concentration is further reduced to 0.1 M (Fig. 2g), and the Stern layer becomes completely amorphous. While the threshold for Wigner crystal-like structures to form on polycrystalline gold in $MgCl_2$ lies between 0.2 and 0.3 M Mg^{2+} at – 0.3 V, it is somewhat higher than 0.7 M Cl^- at + 0.3V.

281

282 **Molecular Dynamics (MD) Simulations of Ion Adsorption to Gold**

283 To gain insight into the structure of the Wigner crystal-like structures at for $MgCl_2$ solutions at
284 gold electrodes, MD simulations with different potentials were completed. To compensate for
285 the limited size and timescales available to MD, as well as the finite reservoir of ions in the
286 simulation box compared to a real system, ion concentration and applied potentials were
287 increased (see Supplementary Note 1 (SI) for simulation details).

288

289 Fig. 3a shows that in the absence of an applied potential ions adsorb mostly in isolation but
290 some ion pairs are present at the interface. When a potential is applied, larger ion aggregates
291 form, with the aggregates increase in size with both applied voltage (Fig. 3b,c) and simulation
292 time (Fig. 3d). These clusters generally consist of alternating Mg^{2+}-Cl^- chains (Fig. 3b–c) which
293 evolve into 2D structures at longer simulation time (Fig. 3d). The clusters are separated from
294 the surface by a water layer (Fig. 3g and the density profiles in Fig. S18a) and not in direct
295 contact or in registry with the gold surface lattice, meaning the ion clusters develop non-
296 epitaxially.

297

298 Several $MgCl_2$ concentrations were simulated (Fig. 3e–f, see Table S1 for the full dataset),
299 which all show the same statistical results. Firstly, the voltage-induced clusters
300 predominantly form at the interface rather than in the bulk, especially for larger clusters (Fig.
301 3e, Fig. S19e,g). Secondly, the lifetimes of the clusters increases with the applied voltage
302 (Fig. 3f, Fig. S19f,h). Thirdly, the distance between (next-nearest neighbor) ions of the same
303 type in clusters along the interface is 2.90 ± 0.18 Å, and independent of cluster size (Fig.
304 3g,h). Fourthly, there is a minimum ion concentration for cluster formation (Fig. S20a,b).
305 Corresponding results were obtained for simulations performed with fluctuating charges on

the gold surface (Fig. S18b). This shows that if the polarizability of the surface is accounted for the voltage required for cluster formation is decreased. The lack of electron exchange in these MD simulation shows cluster formation can occur physically under the influence of the electric field and not via electrochemical processes.

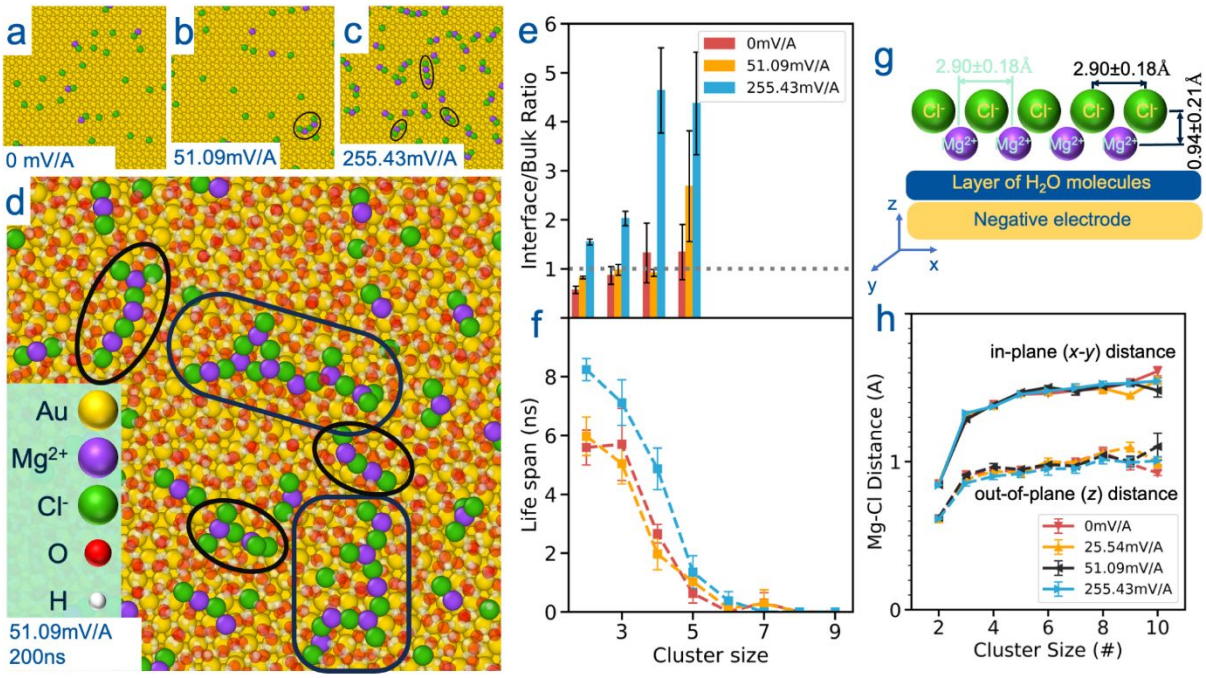

Fig. 3. Computer simulations of gold-electrolyte interface under applied electrical potential. For symmetry, the $MgCl_2$ solution is placed between two gold plates located 6 nm apart (see Supplementary Note 1 in SI) with a voltage applied between the gold plates. In a 2.85 M $MgCl_2$ solution, the number of ionic clusters forming at the interface progressively increases with the applied potential from (a) 0 mV/A to (b) 51.09 mV/A and (c) 255.43 mV/A, and with the simulation time from (a) 10 ns to (d) 200 ns where 2D-like structures are formed. The interface is defined as the region within 5.5 Å of the gold surface for (a–c) and 7.5 Å for (d). The interfacial water molecules are shown semi-transparent in (d) with the ionic clusters highlighted using black circles. Similar results are obtained at lower concentration (0.71 M $MgCl_2$) with the number ratio of clusters forming at the interface and in the bulk significantly increasing with the applied voltage (e). The voltage also stabilizes larger clusters for longer life spans (f, see also Figs. S22 and S23 for full statistics) especially at the interface. At 0.71 M $MgCl_2$, clusters larger than 5 ions are not stable enough (i.e. short life span) to provide meaningful statistics. Larger clusters are however common in 2.85 M $MgCl_2$ (Fig. S19h). The ionic distribution near the negative electrode shows the presence of a layer of water above the electrode, and Mg^{2+} and Cl^- layers further from the surface (g, see also Fig.

S18a). The ion-ion distance is independent of the cluster size for clusters larger than 4 ions and the average distance between the ionic layers and between neighboring Cl^- ions are 0.94 ± 0.21 Å and 2.90 ± 0.18 Å, respectively (g,h).

Ionic density profiles normal to the surface (Fig. S18a, middle and bottom panels) provide clues to the molecular mechanism underpinning the field-induced formation of clusters. At 0 V, the Cl^- and Mg^{2+} ions are preferentially located in and above the water layer, respectively. Application of a negative potential increases the Mg^{2+} density, resulting in a sharp peak close to the surface in the ion distribution profile. This is accompanied by a depletion of Cl^-, which instead forms a dense layer immediately above the Mg^{2+} layer (Fig. 3g). The picture that emerges is of Mg^{2+} and Cl^- ions concentrated in two separate layers ~ 0.94 Å apart (Fig. 3h), closer together than in the absence of applied voltage, thus facilitating the formation of clusters. Both layers are separated from the negative electrode by a water layer, which enables Mg^{2+}–Cl^- clusters to form non-epitaxially. The distance between the smallest features in the AFM images for $MgCl_2$ on the polycrystalline gold surface (Fig. 1) of ~2.8 Å is consistent with the distance between two neighboring Mg^{2+} or Cl^- atoms in the simulation cluster of ~ 2.9 Å. As the number of cations and anions in clusters is approximately equal, the net charge on clusters is positive (each Mg^{2+} Cl^- ion pair has a net +1 charge) which is consistent with overcharging of the surface by the Mg^{2+} counterion, and the physical ion adsorption model where ion correlations lead to Wigner crystal-like structures. AFM images did not reveal Cl^- co-ions adsorbed to the Mg^{2+} Wigner crystal-like structures using either silica-coated or diamond-coated AFM tips. This suggests that chloride is weakly associated with the Mg^{2+} and displaced by the AFM tip during imaging, and rapidly returns to the crystal surface as the tip passes. This is not unexpected, as co-ion adsorption cannot be detected with AFM even on strongly templating crystalline surfaces at low to moderate electrolyte concentrations.[20,45,67–69] At very high electrolyte concentrations (3–5 M) on mica AFM has revealed a co-ion layer,[25] and

resonant anomalous X-ray reflectivity of the interface of mica with rubidium halide solutions revealed co-ion rich second layers.[70] The authors of the latter paper concluded that anion adsorption stabilizes the correlated cation arrangements in the Stern layer. Although for a crystalline mica surface, these results are consistent with the Wigner crystal-like structures proposed in this paper for disordered substrates.

As positive potential is increased, chloride remains concentrated just above the water layer on the gold surface, followed by a Mg^{2+} layer, and Mg^{2+}–Cl^{-} ion clusters also form in this this region (Fig. S18a).

The simulations show the clusters nucleate and progressively grow (compare Fig. 3b with longest simulation in Fig. 3d and Fig. S21c). However, unlike in the AFM images in Figs. 1 and 2, the clusters are never observed in simulations to grow sufficiently to cover large areas of the surface. This is likely a consequence of the simulation length and the limited availability of ions from the solution.

The results of these simulations support the interpretation of the high-resolution AFM images on gold as arising from Wigner crystal-like in-plane ion correlated Stern layer structures. That these do not arise epitaxially from crystalline order in the underlying solid, and may form above a water layer, suggests that they should also form for a variety of electrolytes on a wide variety of amorphous substrates under suitable conditions. In order to test the generality of the findings, we have conducted high-resolution AFM imaging of two naturally charged amorphous surfaces in electrolytes.

High-resolution AFM of amorphous oxide interfaces

The general agreement between the between the AFM and MD provides clear evidence for Wigner crystal-like correlated ionic structures on gold. To investigate the generality of these findings we performed high-resolution AFM imaging of naturally charged amorphous surfaces in various electrolytes.

Silica

Silica is a ubiquitous amorphous substrate[71] whose pH sensitive surface charge is derived from the protonation and deprotonation of Si–OH groups. Fig. 4a compares 10 nm × 10 nm AM-AFM phase images of silica surfaces collected in DI (CO_2-satured) water with 0.38 M $CaCl_2$ and 0.35 M CsCl at pH 9, which is far above the isoelectric point of ~ pH 2 [71] (Fig. 4b–g). The images of the silica surfaces in DI water (Fig. 4a) show randomly arranged bright spherical features due to surface atoms on a gently undulating surface. No ordered packing could be identified in any area at any magnification; The 2D-FFT (inset) is diffuse, which confirms that the surface is amorphous. The RMS roughness of the silica is 15 pm across the 10 nm × 10 nm topography image (Fig. S4), consistent with published values[72].

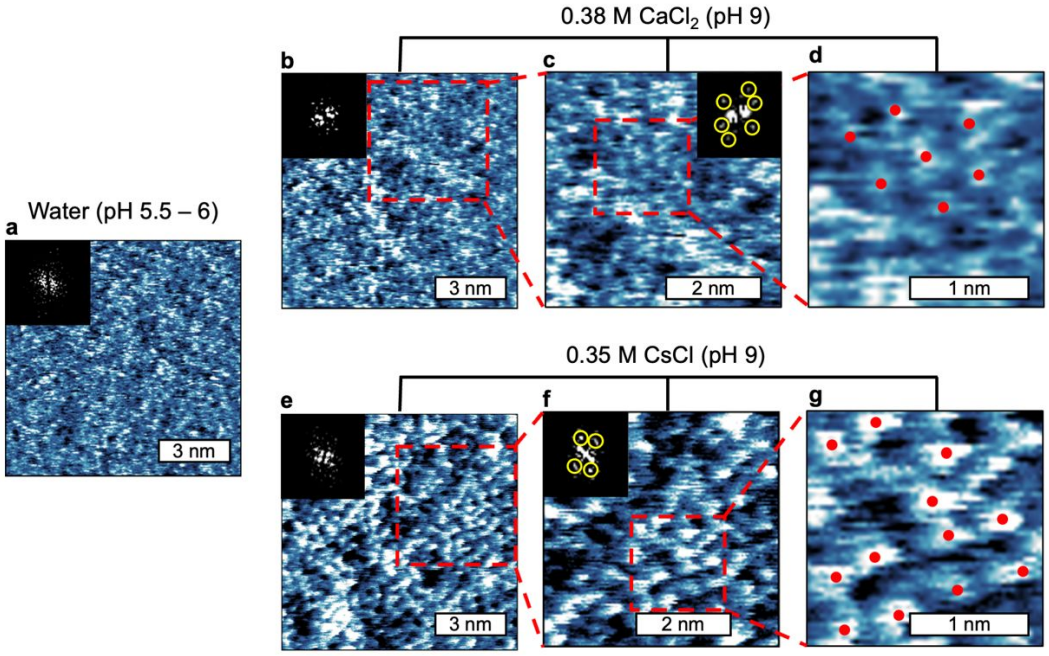

Fig. 4. AFM phase images of the solid/liquid interfaces of silica. (a) Silica in deionized (DI) water. (b–d) 0.38 M $CaCl_2$ at pH 9 (NaOH) and (e–g) 0.35 M CsCl at pH 9 (NaOH) at increasing magnification corresponding to the dashed squares. Insets: 2D-FFT images of the corresponding images; yellow circles in the FFT images highlight the bright spots showing repetitive patterns of the Stern layers. Red dots in the 2 nm × 2 nm images show features aligned in (c) a hexagonally close packed structure and in (g) a square arrangement.

Fig. 4b shows an AM-AFM phase image of a silica surface in 0.38 M $CaCl_2$ at pH 9, which reveals localized crystallinity. The FFT of the higher magnification 5 nm × 5 nm image (Fig. 4c) exhibits three pairs of bright spots consistent with a hexagonal lattice with repeat spacing of 5.5 Å. In the highest magnification 2 nm × 2 nm image red dots have been placed near the center of seven bright features, showing hexagonally arranged ions (Fig. 4c). This indicates that Wigner crystal-like structures of Ca^{2+} form at the amorphous silica/aqueous solution interface.

The FFT for the 5 nm × 5 nm image (Fig. 4c) shows the centers of Ca^{2+} ions are on average 5.5 Å apart, and measurements of individual features show they are 3.0 ± 0.3 Å in diameter. This is much smaller than hydrated Ca^{2+} (8.2 Å[57]) so, like Mg^{2+} on gold, these features likely

correspond to dehydrated Ca^{2+} ions, which is consistent with recent vibrational sum frequency spectroscopy measurements for 0.1 M $CaCl_2$ on silica[73]. These images show that there are 4.25 Ca^{2+} ions/nm^2 (8.5 charges/nm^2) on silica, which exceeds the maximum possible ionized OH group density (Kiselev-Zhuravlev constant) 4.9 OH/nm^2 [74]. The Stern layer Ca^{2+} ions thus overscreen the silica surface charge, which is consistent for conditions on gold for the formation of a Wigner crystal-like structure, and with results for silica particles under similar conditions[73].

At 0.1 M $CaCl_2$, no evidence for Wigner crystal-like structures could be identified on silica (Fig. S4). This is likely because the Ca^{2+} surface excess at 0.1 M is too low for ion correlations to operate despite $\Xi > 10$ for 0.1 M $CaCl_2$. This point is expanded upon below.

Although monovalent, Cs^+ is a weakly hydrated cation, which is expected to favor strong surface adsorption, facilitating AFM imaging. Indeed, AFM images of 0.35 M CsCl at pH 9 (Fig. 4e–g) show clearer features than $CaCl_2$, corresponding to Cs^+ adsorption on negatively charged silica. Strikingly, both the FFT insets in Fig. 4f and 4g, as well as the visible arrangement of the ions in Fig. 4g, reveal square packing of Stern layer Cs^+. The square packing does not persist uninterrupted across the entire image; Fig. 4f and 4g show regions with different symmetry axis directions converge. A square lattice Cs^+ packing is consistent with the primitive cubic crystal structure of solid CsCl but the observed center-to-center distance between Stern layer Cs^+ ions is 8.7 Å, which is more than double the CsCl lattice constant of 4.1 Å. Images for 4 M CsCl at pH 10 on silica (Fig. S5) show that this lattice persists even at very high concentration square Cs^+, with only a modest decrease in center-to-center distance between Stern layer Cs^+ of 8 Å.

436 The images for Cs^+ differ from those for Ca^{2+} in other important ways. The diameter of the
437 features for Cs^+ is 4.1 ± 0.6 Å compared to 3.0 ± 0.3 Å for Ca^{2+}, consistent with the larger ionic
438 radius of Cs^+. The 4.1 ± 0.6 Å feature diameter is also measurably larger than chloride which
439 confirms the Stern layer is Cs^+ enriched. The larger feature size and center-to-center spacing
440 means that 1^+ cesium ions are packed further apart and further from the surface than the smaller
441 Ca^{2+} ions. The Stern layer ion (and charge) density is 3.25 Cs^+ ions/nm^2, which corresponds to
442 a much lower charge density than Ca^{2+} (8.5 charges/nm^2). This is similar in magnitude to that
443 expected for the silica surface, and slightly greater than the 3.1 charges/nm^2 required for Ξ to
444 reach 10.[75] Wigner crystal-like structures for 1^+ ions have not theoretically been predicted,
445 although overcharging by monovalent ions has been reported[32–36]. This result shows that
446 Wigner crystal-like Stern layer structures can form for 1^+ ions even when the surface is not
447 (significantly) overcharged.
448
449 The conditions and type of crystal structure adopted by Stern layer ions is expected to depend
450 on the counter ion charge, surface excess, and hydration, the size difference between the
451 counterion and co-ion, the properties of the surface, and the solid crystal structure of the parent
452 electrolyte. Images for 0.1 M KCl at pH 9 (Fig. S8) clearly different from that for silica in
453 water, confirming K^+ adsorption, but no obvious row directions cannot be identified and the
454 diffuse FFT indicate a lack of crystal order. At high magnification (Fig. S8c) there are hints of
455 local hexagonal close packing (indicated by the red dots on features) but this structure does not
456 persist over large areas. We find no evidence for Wigner crystal-like structures in KCl at
457 concentrations up to 1 M (the highest K^+ concentration examined). The fact that Wigner
458 crystal-like structures can be found for Cs^+ but not K^+ is primarily attributed to strong K^+
459 hydration leading to weaker surface adsorption, but other factors may contribute.
460

GaN

When GaN is exposed to air an oxide layer forms instantaneously, producing a hydroxylated surface[76,77]. The native oxide layer is amorphous[78] due to oxidation-related surface defects and surface reconstructions leading to atomic vacancies, lattice distortion and surface atoms relocating or switching sites[79]. Because the addition of a hydroxyl group to surface Ga is energetically favorable[80], most surface Ga atoms are hydroxylated and, as with silica, pH-dependent protonation and deprotonation produces the surface charge. It would thus be expected that there would be similarities between GaN and silica when imaging in DI water. This can be seen to be true in the image of the GaN surfaces in DI water (Fig. 5a) which consists of randomly arranged spherical features due to surface atoms on an uneven background. The inset 2D-FFT image is diffuse as expected for an amorphous surface. However, the GaN surface RMS roughness is ~49 pm over the 10 nm × 10 nm topography image (see Fig. S1), which is around 3 times higher than silica.

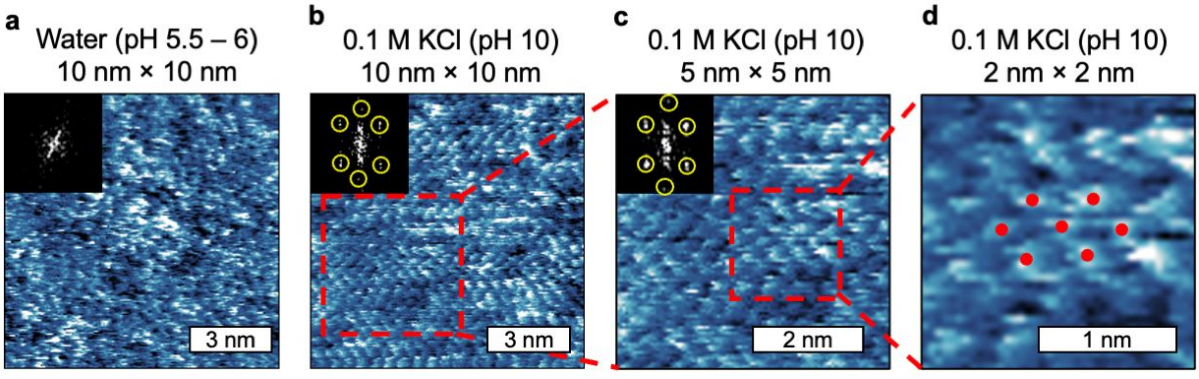

Fig. 5. AFM phase images of the solid/liquid interfaces of gallium nitride (GaN). The images are taken first in deionized (DI) water (a). Then, the images are taken in 0.1M KCl at pH 10 (NaOH) (b–d). The 10 nm × 10 nm image (b) is enlarged to 5 nm × 5 nm (c, corresponding to the dashed square in (b)) and 2 nm × 2 nm (d, corresponding to the dashed squares in (c)). Insets: Corresponding 2D-FFT images; yellow circles in the FFT images highlight the bright spots relating to repetitive patterns of the Stern layers. Red dots in the 2 nm × 2 nm images emphasize features aligned in a hexagonally close packed structure.

Like gold and silica, the GaN surface when imaged in the presence of electrolyte is strikingly different to that in water. Fig. 5b presents 0.1 M KCl on GaN at pH 10, which is far above its isoelectric point of ~ pH 5.5[71,81,82] and so the surface is strongly negatively charged. A clear HCP arrangement of circular features is visible, confirmed by the three pairs of bright spots in the FFT images (inset). This HCP structure is also visible when enlarged to 5 nm × 5 nm (Fig. 5c), and FFT of this higher resolution scan area produces an image almost identical to that at larger scale. The circular features are interpreted to be K^+ ions in the Stern layer of the strongly negatively charged GaN surface[81,82]. In Fig. 5b, the circular features appear 3.4 ± 0.4 Å in diameter, and the average distance between K^+ ions from the FFT is also 3.4 ± 0.5 Å. This feature size is consistent with the average feature size of K^+ on silica of 3.3 ± 0.2 Å and once again similar to bare K^+ ions (3.0 Å [58]), but much smaller than the fully hydrated K^+ diameter (6.6 Å [57]), consistent with a dehydrated and tightly bound layer. The 5 nm × 5 nm (Fig. 5c) and 2 nm × 2 nm (Fig. 5d) zoomed in regions more clearly show the HCP organization of the ions within the Stern layer. The Stern layer ion (charge) density is 5.5 K^+/nm^2. The pH-dependent surface charge of surface-oxidized GaN is comparable to that of titania.[83] Therefore, for a rough comparison, the surface charge density of rutile in 0.3 molal of NaCl at pH 10[84] is ~ 2.25 e/nm^2, which is consistent with the K^+ Wigner-crystal-like structures overcharging the GaN surface.

GaN immersed in 0.1 M $CaCl_2$ solution at pH 10 (Fig. 6c) also yields a Stern layer with the same HCP crystallinity, but the 2.8 ± 0.4 Å feature size is smaller. Similar to the case of K^+, this is consistent with a partial dehydration of the Ca^{2+} ions. Such a high packing density of both ions leaves no space for hydrating water molecules, which can only reside above or below the plane of the ion centers.

Although packing densities of 4.5 ions/nm^2 and periodicity of 3.6 ± 0.1 Å (FFT Fig. 6c) are both lower for the Ca^{2+} than K^+ in the Stern layer on GaN, the Stern layer charge density is higher for Ca^{2+} (9.1 charges/nm^2) than K^+ (5.5 charges/nm^2). This means there must be substantial overcharging by Ca^{2+}, requiring Cl^- ions to be associated with the upper surface of the Wigner crystal-like structure as seen for simulations of Mg^{2+} on gold.

The distance between Stern layer Ca^{2+} ions on GaN is smaller than on silica. This means that the ion surface excess is higher on GaN, even though the solution concentration is lower (0.1 M vs. 0.38 M). This is attributed to GaN having a higher negative charge density at pH 10 than silica at pH 9, so more counterions are attracted into the Stern layer. Stronger ion correlations on GaN gives rise to better defined Wigner crystal-like structures than on silica, and explains why the Ca^{2+} features are smaller for GaN than silica: the volume available for Ca^{2+} vibration (which is what the AFM image measures[20]) is reduced when the interstitial distance is smaller.

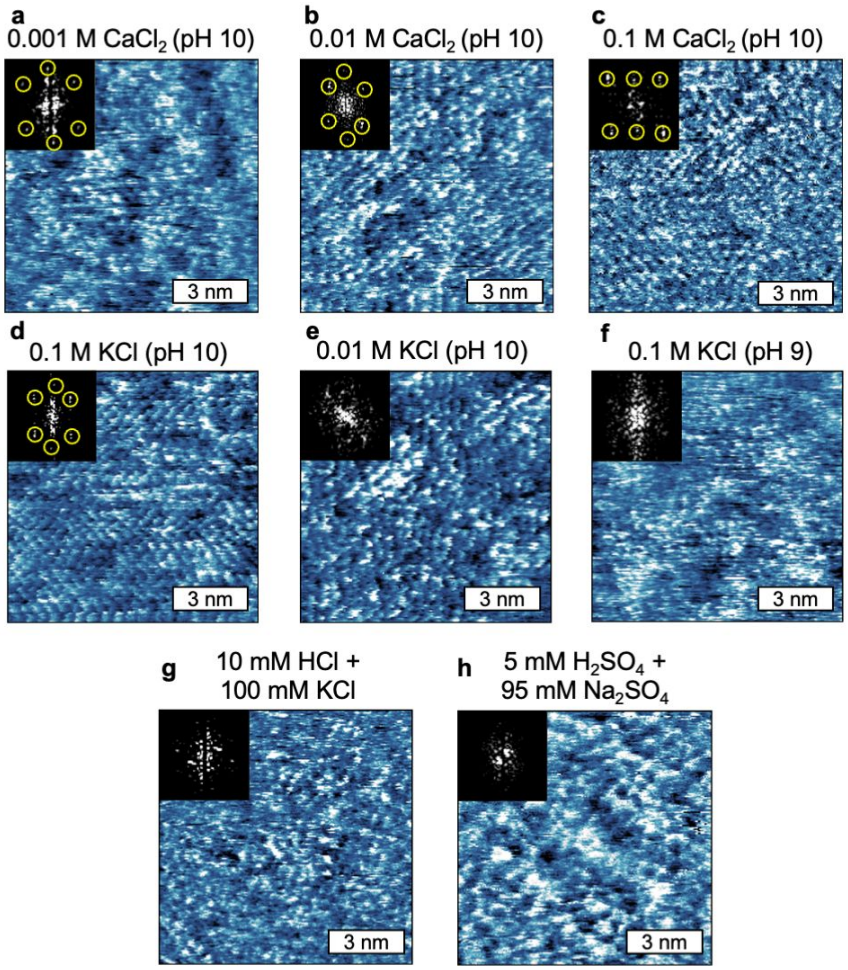

Fig. 6. 10 nm × 10 nm AFM phase images of the interfaces between a gallium nitride (GaN) surface and various solutions as labelled. NaOH was used to achieve alkaline pH. Insets: Corresponding 2D-FFT images for each AFM phase image.

To put these numbers in perspective, it is useful to estimate the surface charge of GaN. While no reported values are directly available as a function of pH and ion concentration, AFM imaging of surfactant adsorption to GaN and related materials[82,85] suggest a similar surface charge to titania (TiO_2) at pH 10. The isoelectric points and surface charging mechanisms[85] of GaN and titania are similar, indicating that the pH-dependent surface charge densities of GaN and TiO_2 are comparable. The surface charge density of the rutile form of titania is ~ 2.25 charges/nm^2 in 0.3 *m* NaCl at pH 10, and 1.75 charges/nm^2 in 0.03 *m* NaCl at pH 10 [84]. It is reasonable to assume the surface charge density of GaN to lie between these two values. By

comparison, the derived Stern layer charge densities for K^+ (5.5 charges/nm^2) and Ca^{2+} (9.1 charges/nm^2) on GaN at pH 10 are at least twice as high, this means the K^+ Stern layer overcharges the GaN surface so, again, chloride must be associated with the upper surface of the Wigner crystal-like structure. For the Ca^{2+} systems, $\Xi \gg 10$, so Wigner crystal-like structures of the divalent ions are expected to form. For the 0.1 M K^+ systems, the existence of Wigner crystal-like structures clearly shows strong correlation, but $\Xi < 10$. Therefore, considering Ξ also fails to predict the non-crystalline Stern layer on silica in 0.1 M $CaCl_2$ at pH 9, this parameter should only serve as an indicator rather than a determiner of whether ion correlations operate in the Stern layer. This shows that the physical mechanism alone is insufficient to explain the formation of Wigner crystal-like structures, and aspects of the chemical model, especially relating to ion surface excess, may apply.

Next the effect of ion species and concentration, and the surface charge, is probed for Stern layers on GaN. For KCl on GaN at pH 10, Wigner crystal-like structures form for 0.1 M KCl but not for 0.01 M KCl (Fig. 6e shows an amorphous Stern layer), so the threshold concentration for the formation of Wigner crystal-like structures lies within these two concentrations at pH 10. Similarly, for 0.1 M KCl, Wigner crystal-like structures are observed at pH 10 but the Stern layer is disordered at pH 9 (Fig. 6f). Some rows of aligned ions are still observed, which leads to the weak spots in the FFT images. This means for 0.1 M KCl on GaN, the threshold surface charge for Wigner crystal-like structures is achieved between pH 9 and pH 10.

Fig. 6a–c shows 10 nm × 10 nm images for 0.001 M, 0.01 M and 0.1 M $CaCl_2$ on GaN at pH 10. Even for 1 mM, HCP Wigner crystal-like structures can be discerned (Fig. 6a), confirmed by the three pairs of bright spots marked with yellow circles in the FFT insets. Images of 0.1

mM $CaCl_2$ on GaN (not shown) have the same appearance of GaN in water. This shows the threshold $CaCl_2$ concentration for Wigner crystal-like structures on GaN at pH 10 is between 0.1 mM and 1 mM. The presence of Wigner crystal-like structures at pH 10 in 0.01 M $CaCl_2$ but not 0.01 M KCl is due to electrostatic attractions between charges on the GaN surface and divalent Ca^{2+} ions being stronger than for monovalent K^+, similar to the case on the silica surface discussed above.

Stern layers of Cl^- (0.11 M Cl^- in total: 10 mM HCl + 100 mM KCl) and SO_4^{2-} (0.1 M SO_4^{2-} in total: 5 mM H_2SO_4 + 95 mM Na_2SO_4) on GaN at pH 2 are presented in Fig. 6g,h. The Stern layers are amorphous, but notably the size difference between Cl^- ions (3.6 ± 0.4 Å) and SO_4^{2-} ions (5.2 ± 0.9 Å) is clear in the phase image, and consistent with reported ion diameters of 3.6 Å and 4.8 Å [57], respectively. This further confirms our hypothesis that the Stern layer ions are imaged. The lower crystallinity of the Stern layer Cl^- ions and SO_4^{2-} ions is primarily attributed to the lower magnitude of the positive surface charge at pH 2 than at pH 10. For the monovalent Cl^- ions, the weaker electrostatics due to its lower valency may also contribute to the reduced Stern layer crystallinity, such as for Cl^- adsorption to gold at positive potentials.

Combined, the AFM results for gold, silica and GaN for a wide range of solution conditions show that Wigner crystal-like structures only form above a threshold Stern layer ion surface excess. Below this threshold, the Stern layers are amorphous.

Conclusions

In situ AM-AFM images have been used to reveal the structure of Stern layer ions at the interface of electrolyte solutions with polycrystalline gold, and amorphous silica and GaN

surfaces. When the density of ions in the Stern layer is low, unstructured Stern layers form. However, when the density of ions in the Stern layer exceeds a system dependent threshold value, the magnitude of lateral repulsions between Stern layer counterions is greater than surface – counterion attractions, and the ions form Wigner crystal-like structures to minimize repulsions. In most cases the Wigner crystal-like structures are hexagonally close packed, but square and worm-like structures were also found. The type of crystal structure adopted by Stern layer ions is likely affected by the properties of the surface, the size difference between the counterion and co-ion, the counter ion charge, surface excess, and hydration, and the solid crystal structure of the electrolyte.

Above the threshold, the charge per area of the Wigner crystal-like structures is much higher than that of the surfaces, which means the surfaces are overcharged. This also means there must be a significant concentration of ions (co-ions to the substrate) associated with the upper surface of the Wigner crystal-like structure. The threshold depends on the surface charge density and, the concentration and valence of the counterion.

Molecular dynamic simulations of the $MgCl_2$ at a gold electrode show that when sufficiently high potential is applied to the surface ion clusters form with dimensions similar to the Wigner crystal-like structures in the AFM images. Mg^{2+} and Cl^- ions are concentrated in two separate layers ~ 0.94 Å apart (Fig. 3h) separated from the negative electrode by a water layer, which enables Mg^{2+}–Cl^- clusters to form non epitaxially. The distance between two neighboring Mg^{2+} or Cl^- atoms in the simulation cluster is consistent with the space between the smallest features in the AFM for the corresponding system. The of cations and anions in clusters is approximately equal so the net charge on clusters is positive. This is therefore consistent with

609 overcharging of the surface by the magnesium counterion, and the physical adsorption model
610 in which ion correlations lead to Wigner crystal-like structures.
611
612 Wigner crystal-like structures have been observed for gold, silica and GaN surfaces, for a
613 variety of ions of different sizes and valence, suggesting it is likely that Wigner crystal-like
614 structures naturally exist at many surfaces in electrolyte solutions. Experimental confirmation
615 of Wigner crystal-like structures resolves a decades-old argument between chemists and
616 physicists regarding the mechanism of surface overcharging in favor of the physical model.
617
618 The ability to image Stern layer ions on amorphous surfaces, and in particular the presence of
619 Wigner crystal-like structures for high electrolyte concentrations and surface charges,
620 represents a step change in our understanding of the overcharging phenomenon, and of the
621 nature of solid / liquid interfaces in general. The type of ions, their concentrations and the
622 surface potentials explored in this study reflect countless real-life systems. We therefore expect
623 our findings to impact across diverse fields including energy storage[86–88], biology/medicine[89,90],
624 chemistry[88,91–93], engineering[86,91,94], environmental science[95,96], and nanotechnology[86,97]. For
625 example, for supercapacitors, a better understanding of the Stern layer can help develop
626 strategies to increase interfacial charge storage density[98] such as by using a mixture of ions
627 with different sizes. For CO_2 reduction, a better understanding and control of the Stern layer
628 structure can help maximize the available surface reaction sites, and thus significantly improve
629 the kinetics of the process[99]. For ion-sensitive field-effect transistors (ISFETs), increasingly
630 used as chemical and biochemical sensors, the Stern layer on the active gate area controls the
631 device conductivity and hence affects the sensitivity, so a better understanding of the Stern
632 layer can help improve their sensitivity[100]. Understanding the lateral Stern layer structure could
633 help better regulate interactions between protein surfaces to prevent coalescence, aiding the

development of stable protein-based pharmaceutical products in liquid form such as vaccines and antibody drugs[12].

Experimental Section

Preparation of the GaN surface

A *c*-plane Ga-polar gallium nitride (GaN) sample of a thickness of ~ 2 μm grown on sapphire (0001) substrates using metal-organic chemical vapor deposition (MOCVD) acquired from Technologies and Devices International, Inc. was used. Before the sample was used, the sample was immersed in acetone and isopropanol at 60 °C for 5 minutes each to remove any organic contamination on the surface and then rinsed in deionized (DI) water for 5 minutes; next, to remove the produce a fresh native oxide layer on the GaN surface, the sample was immersed in 32% hydrochloric acid (HCl) for 5 minutes and rinsed in DI water for 5 minutes. Prior to each AFM experiment, the GaN surface was cleaned with detergent, rinsed with DI water, ethanol, acetone, isopropanol and DI water again, and then dried with compressed air.

Preparation of the silica surface

A silica sample grown on a silicon wafer was sourced from Silicon Valley Microelectronics CA, USA. The surface roughness of the wafer is 5 ± 3 Å. Before use, the silica surface was immersed in concentrated NaOH solution for 5 minutes and rinsed with DI water. Prior to each AFM experiment, the silica surface was cleaned with 0detergent, rinsed with DI water, cleaned in a UV/ozone cleaner for ~ 15 minutes, rinsed with ethanol and DI water again, and then dried with compressed air.

Preparation of the gold surface

Au(111) films of a thickness of 300 nm deposited on mica substrates with atomically smooth surfaces were purchased from Georg Albert PVD – Beschichtungen, Germany. Prior to each AFM experiment, the gold surface was cleaned in a UV/ozone cleaner for ~ 15 min, rinsed with ethanol and DI water, and dried with compressed air. An electrode is attached to the gold surface using MG Chemicals silver conductive epoxy adhesive 8331 so that the surface is also used as a working electrode during AFM imaging.

AFM experiments

AFM imaging in this work was achieved using a Cypher VRS system (Asylum Research, Oxford Instruments, USA) with a liquid perfusion cantilever holder and a heater-cooler sample stage. Silica AFM probes FS-1500AuD (Asylum Research, USA) and Arrow UHFAuD (NanoWorld, Switzerland) with spring constants ranging between 5 and 11 N/m were used at resonance frequencies ranging from ~ 300 kHz to ~ 600 kHz in aqueous solutions. Diamond AFM probes (Adama Super Sharp AD-2.8-SS, Ireland) with spring constants around 1.7 N/m were used at the second eigenmode (~ 110 kHz). The cantilevers were calibrated using the thermal method[101].

For the AFM experiments with a gold surface, a simple electrochemical cell was built based on the Cypher perfusion cantilever holder: the gold surface acted as the working electrode; a platinum wire was fed through the liquid exchange ports on the liquid perfusion cell and acted as the counter electrode and pseudo-reference electrode. The AFM experiments were conducted within the electrochemical window of the liquid, so no appreciable current was observed.

Prior to each AFM measurement, the AFM probe was cleaned using a UV/ozone cleaner for ~ 10 minutes; the cantilever holder was cleaned with ethanol and DI water and then dried with ultra-high-purity nitrogen. 40 – 80 μL of the liquid to be tested are added to the AFM tip and the surface so that the tip and the surface are fully immersed in the liquid. After a liquid is added to the system, the AFM was left for at least 20 minutes to reach thermal equilibrium. Then, AFM images of the Stern layers were captured.

All the high-resolution AFM images presented were captured in amplitude modulation (AM) mode with the cantilever and the sample surface immersed in aqueous solutions at 25 °C. In AM mode, the AFM cantilever was excited photothermally and oscillated. Free amplitude (A_0) is an amplitude at which the AFM tip oscillates near its resonance frequency in the liquid with no influence from the surface. A_0 can be adjusted by the user through a drive amplitude which controls the intensity of the laser exciting the AFM cantilever. The tip gradually approaches the surface, causing the oscillating amplitude of the cantilever to decrease due to tip–surface interaction until reaching a user-defined working amplitude (A) at which the AFM images are captured. The A/A_0 ratio was kept between 0.4 and 0.6. At a higher A/A_0 ratio, the tip–surface distance is too great, and the force applied on the tip is insufficient to capture the Stern layer structure at an acceptable resolution; at a lower A/A_0 ratio, the tip displaces the adsorbed ions with high force, and the bare sample surface is imaged[22]. At an extremely low A/A_0 ratio, the tip will be almost in contact with the surface, resembling contact-mode imaging. Representative images are presented in the article. All the images have been treated with the Gwyddion software using the following series of data processing operations: level data by mean plain subtraction, align rows using polynomial (degree 3), remove polynomial background (horizontal and vertical polynomial degrees 3) and then adjust the color range with tails cut off.

Supporting Information

The Supporting Information is available free of charge at [URL].

Simulation details; Further details on AFM phase and topography images; Further details on AFM images acquired with different AFM probes and different solvents; Discussion on the role of solvent in ion adsorption; Details on the surface excess and percentage by volume of adsorbed ions; Supplementary AFM images; Simulation setup and results (PDF)

Acknowledgements

This work was partially funded by the Australian Research Council Discovery Project grant (DP200102248) and Linkage Infrastructure, Equipment and Facilities grant (LE200100162). JW was funded by a Scholarship for International Research Fees (SIRF) and a University Postgraduate Award (UPA) provided by the Australian Government and The University of Western Australia. JW, HL and RA acknowledge the facilities, and the scientific and technical assistance of the Australian Microscopy & Microanalysis Research Facility at the Centre for Microscopy, Characterisation & Analysis, The University of Western Australia, a facility funded by the University, State and Commonwealth Governments. KV and MT acknowledge funding from the Engineering and Physical Sciences Research Council (EP/S028234/1). This work has made use of the Hamilton HPC Service of Durham University.

References

(1) Israelachvili, J. N. Chapter 14 - Electrostatic Forces between Surfaces in Liquids. In *Intermolecular and Surface Forces*; Israelachvili, J. N. B. T.-I. and S. F. (Third E., Ed.; Academic Press: San Diego, 2011; pp 291–340. https://doi.org/https://doi.org/10.1016/B978-0-12-375182-9.10014-4.

(2) Gonella, G.; Backus, E. H. G.; Nagata, Y.; Bonthuis, D. J.; Loche, P.; Schlaich, A.; Netz, R. R.; Kühnle, A.; McCrum, I. T.; Koper, M. T. M.; Wolf, M.; Winter, B.; Meijer, G.; Campen, R. K.; Bonn, M. Water at Charged Interfaces. *Nature Reviews Chemistry*. Nature Publishing Group June 24, 2021, pp 466–485. https://doi.org/10.1038/s41570-021-00293-2.

(3) Helmholtz, H. Ueber Einige Gesetze Der Vertheilung Elektrischer Ströme in Körperlichen Leitern, Mit Anwendung Auf Die Thierisch-elektrischen Versuche (Schluss.). *Ann. der Phys. und Chemie* **1853**, *165* (7), 353–377. https://doi.org/10.1002/andp.18531650702.

(4) Chapman, D. L. LI. A Contribution to the Theory of Electrocapillarity. *London, Edinburgh, Dublin Philos. Mag. J. Sci.* **1913**, *25* (148), 475–481. https://doi.org/10.1080/14786440408634187.

(5) Gouy, M. Sur La Constitution de La Charge Électrique à La Surface d'un Électrolyte. *J. Phys. Théorique Appliquée* **1910**, *9* (1), 457–468. https://doi.org/10.1051/jphystap:019100090045700.

(6) Stern, O. Zur Theorie Der Elektrolytischen Doppelschicht. *Zeitschrift für Elektrochemie und Angew. Phys. Chemie* **1924**, *30* (21–22), 508–516. https://doi.org/10.1002/BBPC.192400182.

(7) Grahame, D. C. The Electrical Double Layer and the Theory of Electrocapillarity. *Chem. Rev.* **1947**, *41* (3), 441–501. https://doi.org/10.1021/cr60130a002.

(8) Wang, X.; Liu, K.; Wu, J. Demystifying the Stern Layer at a Metal-Electrolyte Interface: Local Dielectric Constant, Specific Ion Adsorption, and Partial Charge Transfer. *J. Chem. Phys.* **2021**, *154* (12), 124701. https://doi.org/10.1063/5.0043963.

(9) Hiemstra, T.; Van Riemsdijk, W. H. On the Relationship between Charge Distribution, Surface Hydration, and the Structure of the Interface of Metal Hydroxides. *J. Colloid*

Interface Sci. **2006**, *301* (1), 1–18. https://doi.org/10.1016/j.jcis.2006.05.008.

(10) Leroy, P.; Revil, A. A Triple-Layer Model of the Surface Electrochemical Properties of Clay Minerals. *J. Colloid Interface Sci.* **2004**, *270* (2), 371–380. https://doi.org/10.1016/j.jcis.2003.08.007.

(11) Bourg, I. C.; Lee, S. S.; Fenter, P.; Tournassat, C. Stern Layer Structure and Energetics at Mica-Water Interfaces. *J. Phys. Chem. C* **2017**, *121* (17), 9402–9412. https://doi.org/10.1021/acs.jpcc.7b01828.

(12) Finney, A. R.; McPherson, I. J.; Unwin, P. R.; Salvalaglio, M. Electrochemistry, Ion Adsorption and Dynamics in the Double Layer: A Study of NaCl(Aq) on Graphite. *Chem. Sci.* **2021**, *12* (33), 11166–11180. https://doi.org/10.1039/d1sc02289j.

(13) Preočanin, T.; Selmani, A.; Lindqvist-Reis, P.; Heberling, F.; Kallay, N.; Lützenkirchen, J. Surface Charge at Teflon/Aqueous Solution of Potassium Chloride Interfaces. *Colloids Surfaces A Physicochem. Eng. Asp.* **2012**, *412*, 120–128. https://doi.org/10.1016/j.colsurfa.2012.07.025.

(14) Beattie, J. K.; Djerdjev, A. M. The Pristine Oil/Water Interface: Surfactant-Free Hydroxide-Charged Emulsions. *Angew. Chemie Int. Ed.* **2004**, *43* (27), 3568–3571. https://doi.org/10.1002/ANIE.200453916.

(15) Roberts, D.; Keeling, R.; Tracka, M.; Van Der Walle, C. F.; Uddin, S.; Warwicker, J.; Curtis, R. The Role of Electrostatics in Protein-Protein Interactions of a Monoclonal Antibody. *Mol. Pharm.* **2014**, *11* (7), 2475–2489. https://doi.org/10.1021/mp5002334.

(16) Stigter, D. Micelle Formation by Ionic Surfactants. III. Model of Stern Layer, Ion Distribution, and Potential Fluctuations. *J. Phys. Chem.* **1975**, *79* (10), 1008–1014. https://doi.org/10.1021/j100577a013.

(17) Klausen, L. H.; Fuhs, T.; Dong, M. Mapping Surface Charge Density of Lipid Bilayers by Quantitative Surface Conductivity Microscopy. *Nat. Commun.* **2016**, *7* (1), 1–10.

https://doi.org/10.1038/ncomms12447.

(18) Meegoda, J. N.; Hewage, S. A.; Batagoda, J. H. Application of the Diffused Double Layer Theory to Nanobubbles. *Langmuir* **2019**, *35* (37), 12100–12112. https://doi.org/10.1021/acs.langmuir.9b01443.

(19) Bockris, J. O.; Devanathan, M. A.; Müller, K. On the Structure of Charged Interfaces. *Proc. R. Soc. London. Ser. A. Math. Phys. Sci.* **1963**, *274* (1356), 55–79. https://doi.org/10.1098/rspa.1963.0114.

(20) Loh, S.-H.; Jarvis, S. P. Visualization of Ion Distribution at the Mica−Electrolyte Interface. *Langmuir* **2010**, *26* (12), 9176–9178. https://doi.org/10.1021/la1011378.

(21) Ricci, M.; Trewby, W.; Cafolla, C.; Voïtchovsky, K. Direct Observation of the Dynamics of Single Metal Ions at the Interface with Solids in Aqueous Solutions. *Sci. Rep.* **2017**, *7* (1), 1–12. https://doi.org/10.1038/srep43234.

(22) Ricci, M.; Spijker, P.; Stellacci, F.; Molinari, J. F.; Voïtchovsky, K. Direct Visualization of Single Ions in the Stern Layer of Calcite. *Langmuir* **2013**, *29* (7), 2207–2216. https://doi.org/10.1021/la3044736.

(23) Ricci, M.; Spijker, P.; Voïtchovsky, K. Water-Induced Correlation between Single Ions Imaged at the Solid-Liquid Interface. *Nat. Commun.* **2014**, *5* (1), 1–8. https://doi.org/10.1038/ncomms5400.

(24) Martin-Jimenez, D.; Garcia, R. Identification of Single Adsorbed Cations on Mica-Liquid Interfaces by 3D Force Microscopy. *J. Phys. Chem. Lett.* **2017**, *8* (23), 5707–5711. https://doi.org/10.1021/acs.jpclett.7b02671.

(25) Martin-Jimenez, D.; Chacon, E.; Tarazona, P.; Garcia, R. Atomically Resolved Three-Dimensional Structures of Electrolyte Aqueous Solutions near a Solid Surface. *Nat. Commun.* **2016**, *7* (1), 1–7. https://doi.org/10.1038/ncomms12164.

(26) Siretanu, I.; Ebeling, D.; Andersson, M. P.; Stipp, S. L. S.; Philipse, A.; Stuart, M. C.;

807 Van Den Ende, D.; Mugele, F. Direct Observation of Ionic Structure at Solid-Liquid
808 Interfaces: A Deep Look into the Stern Layer. *Sci. Rep.* **2014**, *4* (1), 1–7.
809 https://doi.org/10.1038/srep04956.
810 (27) Hartkamp, R.; Siboulet, B.; Dufrêche, J. F.; Coasne, B. Ion-Specific Adsorption and
811 Electroosmosis in Charged Amorphous Porous Silica. *Phys. Chem. Chem. Phys.* **2015**,
812 *17* (38), 24683–24695. https://doi.org/10.1039/c5cp03818a.
813 (28) Packham, R. F. Some Studies of the Coagulation of Dispersed Clays with Hydrolyzing
814 Salts. *J. Colloid Sci.* **1965**, *20* (1), 81–92. https://doi.org/10.1016/0095-8522(65)90094-
815 2.
816 (29) Matijević, E.; Janauer, G. E. Coagulation and Reversal of Charge of Lyophobic Colloids
817 by Hydrolyzed Metal Ions II. Ferric Nitrate. *J. Colloid Interface Sci.* **1966**, *21* (2), 197–
818 223. https://doi.org/10.1016/0095-8522(66)90034-1.
819 (30) James, R. O.; Healy, T. W. Adsorption of Hydrolyzable Metal Ions at the Oxide-Water
820 Interface. I. Co(II) Adsorption on SiO2 and TiO2 as Model Systems. *J. Colloid Interface*
821 *Sci.* **1972**, *40* (1), 42–52. https://doi.org/10.1016/0021-9797(72)90172-5.
822 (31) Breeuwsma, A.; Lyklema, J. Physical and Chemical Adsorption of Ions in the Electrical
823 Double Layer on Hematite (α-Fe2O3). *J. Colloid Interface Sci.* **1973**, *43* (2), 437–448.
824 https://doi.org/10.1016/0021-9797(73)90389-5.
825 (32) Kosmulski, M. Oxide/Electrolyte Interface: Electric Double Layer in Mixed Solvent
826 Systems. *Colloids and Surfaces A: Physicochemical and Engineering Aspects*. Elsevier
827 February 20, 1995, pp 81–100. https://doi.org/10.1016/0927-7757(94)03029-Y.
828 (33) Kosmulski, M.; Matijević, E. Zeta Potential of Anatase (TiO2) in Mixed Solvents.
829 *Colloids and Surfaces* **1992**, *64* (1), 57–65. https://doi.org/10.1016/0166-
830 6622(92)80162-U.
831 (34) Kosmulski, M.; Rosenholm, J. B. Electroacoustic Study of Adsorption of Ions on

832 Anatase and Zirconia from Very Concentrated Electrolytes. *J. Phys. Chem.* **1996**, *100*
833 (28), 11681–11687. https://doi.org/10.1021/jp960315u.
834 (35) Gustafsson, J.; Mikkola, P.; Jokinen, M.; Rosenholm, J. B. The Influence of PH and
835 NaCl on the Zeta Potential and Rheology of Anatase Dispersions. *Colloids Surfaces A*
836 *Physicochem. Eng. Asp.* **2000**, *175* (3), 349–359. https://doi.org/10.1016/S0927-
837 7757(00)00634-8.
838 (36) Lee, S. S.; Koishi, A.; Bourg, I. C.; Fenter, P. Ion Correlations Drive Charge
839 Overscreening and Heterogeneous Nucleation at Solid-Aqueous Electrolyte Interfaces.
840 *Proc. Natl. Acad. Sci. U. S. A.* **2021**, *118* (32), 2105154118.
841 https://doi.org/10.1073/pnas.2105154118.
842 (37) Lyklema, J. Quest for Ion-Ion Correlations in Electric Double Layers and Overcharging
843 Phenomena. *Advances in Colloid and Interface Science*. Elsevier March 1, 2009, pp
844 205–213. https://doi.org/10.1016/j.cis.2008.12.002.
845 (38) Lyklema, J. Overcharging, Charge Reversal: Chemistry or Physics? *Colloids Surfaces*
846 *A Physicochem. Eng. Asp.* **2006**, *291* (1–3), 3–12.
847 https://doi.org/10.1016/j.colsurfa.2006.06.043.
848 (39) de Vos, W. M.; Lindhoud, S. Overcharging and Charge Inversion: Finding the Correct
849 Explanation(S). *Advances in Colloid and Interface Science*. Elsevier December 1, 2019,
850 p 102040. https://doi.org/10.1016/j.cis.2019.102040.
851 (40) Grosberg, A. Y.; Nguyen, T. T.; Shklovskii, B. I. *Colloquium: The Physics of Charge*
852 *Inversion in Chemical and Biological Systems*; American Physical Society, 2002; Vol.
853 74, pp 329–345. https://doi.org/10.1103/RevModPhys.74.329.
854 (41) Jiménez, M. L.; Delgado, Á. V.; Lyklema, J. Hydrolysis versus Ion Correlation Models
855 in Electrokinetic Charge Inversion: Establishing Application Ranges. *Langmuir* **2012**,
856 *28* (17), 6786–6793. https://doi.org/10.1021/la3010773.

857 (42) Semenov, I.; Raafatnia, S.; Sega, M.; Lobaskin, V.; Holm, C.; Kremer, F.
858 Electrophoretic Mobility and Charge Inversion of a Colloidal Particle Studied by Single-
859 Colloid Electrophoresis and Molecular Dynamics Simulations. *Phys. Rev. E - Stat.*
860 *Nonlinear, Soft Matter Phys.* **2013**, *87* (2), 022302.
861 https://doi.org/10.1103/PhysRevE.87.022302.
862 (43) Voïtchovsky, K. Anharmonicity, Solvation Forces, and Resolution in Atomic Force
863 Microscopy at the Solid-Liquid Interface. *Phys. Rev. E - Stat. Nonlinear, Soft Matter*
864 *Phys.* **2013**, *88* (2), 022407. https://doi.org/10.1103/PhysRevE.88.022407.
865 (44) Fukuma, T.; Garcia, R. Atomic- and Molecular-Resolution Mapping of Solid-Liquid
866 Interfaces by 3D Atomic Force Microscopy. *ACS Nano*. American Chemical Society
867 December 26, 2018, pp 11785–11797. https://doi.org/10.1021/acsnano.8b07216.
868 (45) Siretanu, I.; Ebeling, D.; Andersson, M. P.; Stipp, S. L. S.; Philipse, A.; Stuart, M. C.;
869 Van Den Ende, D.; Mugele, F. Direct Observation of Ionic Structure at Solid-Liquid
870 Interfaces: A Deep Look into the Stern Layer. *Sci. Rep.* **2014**, *4*, 19–21.
871 https://doi.org/10.1038/srep04956.
872 (46) Schulz, J. C.; Warr, G. G. Adsorbed Layer Structure of Cationic Surfactants on Clays
873 (Mica Is Not a Typical Substrate for Adsorption Studies). *Langmuir* **2000**, *16* (7), 2995–
874 2996. https://doi.org/10.1021/la9912747.
875 (47) Jal, P. K.; Patel, S.; Mishra, B. K. Chemical Modification of Silica Surface by
876 Immobilization of Functional Groups for Extractive Concentration of Metal Ions.
877 *Talanta* **2004**, *62* (5), 1005–1028. https://doi.org/10.1016/j.talanta.2003.10.028.
878 (48) Steinhoff, G.; Hermann, M.; Schaff, W. J.; Eastman, L. F.; Stutzmann, M.; Eickhoff, M.
879 PH Response of GaN Surfaces and Its Application for PH-Sensitive Field-Effect
880 Transistors. *Appl. Phys. Lett.* **2003**, *83* (1), 177–179. https://doi.org/10.1063/1.1589188.
881 (49) Kudo, A.; Miseki, Y. Heterogeneous Photocatalyst Materials for Water Splitting. *Chem.*

882 *Soc. Rev.* **2009**, *38* (1), 253–278. https://doi.org/10.1039/B800489G.
883 (50) Sperelakis, N. Basis of the Resting Potential. In *Physiology and Pathophysiology of the*
884 *Heart*; Sperelakis, N., Ed.; Springer US: Boston, MA, 1989; pp 59–80.
885 https://doi.org/10.1007/978-1-4613-0873-7_3.
886 (51) Labuda, A.; Hohlbauch, S.; Kocun, M.; Limpoco, F. T.; Kirchhofer, N.; Ohler, B.;
887 Hurley, D. Tapping Mode AFM Imaging in Liquids with BlueDrive Photothermal
888 Excitation. *Micros. Today* **2018**, *26* (6), 12–17.
889 https://doi.org/10.1017/s1551929518001050.
890 (52) García, R. Instrumental and Conceptual Aspects. In *Amplitude Modulation Atomic*
891 *Force Microscopy*; Wiley Online Books; Wiley-VCH Verlag GmbH & Co. KGaA:
892 Weinheim, Germany, 2010; pp 9–24. https://doi.org/10.1002/9783527632183.ch2.
893 (53) Tao, N. J.; Lindsay, S. M. Observations of the 22×√3 Reconstruction of Au(111) under
894 Aqueous Solutions Using Scanning Tunneling Microscopy. *J. Appl. Phys.* **1991**, *70* (9),
895 5141–5143. https://doi.org/10.1063/1.348991.
896 (54) Hasegawa, Y.; Avouris, P. Manipulation of the Reconstruction of the Au(111) Surface
897 with the STM. *Science (80-.).* **1992**, *258* (5089), 1763–1765.
898 https://doi.org/10.1126/science.258.5089.1763.
899 (55) Elbourne, A.; McDonald, S.; Voïchovsky, K.; Endres, F.; Warr, G. G.; Atkin, R.
900 Nanostructure of the Ionic Liquid-Graphite Stern Layer. *ACS Nano* **2015**, *9* (7), 7608–
901 7620. https://doi.org/10.1021/acsnano.5b02921.
902 (56) McDonald, S.; Elbourne, A.; Warr, G. G.; Atkin, R. Metal Ion Adsorption at the Ionic
903 Liquid-Mica Interface. *Nanoscale* **2016**, *8* (2), 906–914.
904 https://doi.org/10.1039/c5nr05833c.
905 (57) Nightingale, E. R. Phenomenological Theory of Ion Solvation. Effective Radii of
906 Hydrated Ions. *J. Phys. Chem.* **1959**, *63* (9), 1381–1387.

907 https://doi.org/10.1021/j150579a011.
908 (58) Shannon, R. D. Revised Effective Ionic Radii and Systematic Studies of Interatomic
909 Distances in Halides and Chalcogenides. *Acta Crystallogr. Sect. A* **1976**, *32* (5), 751–
910 767. https://doi.org/10.1107/S0567739476001551.
911 (59) Moreira, A. G.; Netz, R. R. Binding of Similarly Charged Plates with Counterions Only.
912 *Phys. Rev. Lett.* **2001**, *87* (7), 78301. https://doi.org/10.1103/PhysRevLett.87.078301.
913 (60) Comtet, J.; Niguès, A.; Kaiser, V.; Coasne, B.; Bocquet, L.; Siria, A. Nanoscale
914 Capillary Freezing of Ionic Liquids Confined between Metallic Interfaces and the Role
915 of Electronic Screening. *Nat. Mater.* **2017**, *16* (6), 634–639.
916 https://doi.org/10.1038/nmat4880.
917 (61) Scalfi, L.; Dufils, T.; Reeves, K. G.; Rotenberg, B.; Salanne, M. A Semiclassical
918 Thomas-Fermi Model to Tune the Metallicity of Electrodes in Molecular Simulations.
919 *J. Chem. Phys.* **2020**, *153* (17), 174704. https://doi.org/10.1063/5.0028232.
920 (62) Li, Z.; Ruiz, V. G.; Kanduč, M.; Dzubiella, J. Highly Heterogeneous Polarization and
921 Solvation of Gold Nanoparticles in Aqueous Electrolytes. *ACS Nano* **2021**, *15* (8),
922 13155–13165. https://doi.org/10.1021/acsnano.1c02668.
923 (63) Serva, A.; Scalfi, L.; Rotenberg, B.; Salanne, M. Effect of the Metallicity on the
924 Capacitance of Gold-Aqueous Sodium Chloride Interfaces. *J. Chem. Phys.* **2021**, *155*
925 (4), 44703. https://doi.org/10.1063/5.0060316.
926 (64) Chakravarty, S.; Kivelson, S.; Nayak, C.; Voelker, K. Wigner Glass, Spin Liquids and
927 the Metal-Insulator Transition. *Philos. Mag. B Phys. Condens. Matter; Stat. Mech.*
928 *Electron. Opt. Magn. Prop.* **1999**, *79* (6), 859–868.
929 https://doi.org/10.1080/13642819908214845.
930 (65) Voelker, K.; Chakravarty, S. Multiparticle Ring Exchange in the Wigner Glass and Its
931 Possible Relevance to Strongly Interacting Two-Dimensional Electron Systems in the

932 Presence of Disorder. *Phys. Rev. B - Condens. Matter Mater. Phys.* **2001**, *64* (23),
933 2351251–23512515. https://doi.org/10.1103/physrevb.64.235125.
934 (66) Reichhardt, C.; Olson, C. J.; Grønbech-Jensen, N.; Nori, F. Moving Wigner Glasses and
935 Smectics: Dynamics of Disordered Wigner Crystals. *Phys. Rev. Lett.* **2001**, *86* (19),
936 4354–4357. https://doi.org/10.1103/PhysRevLett.86.4354.
937 (67) Ebeling, D.; Solares, S. D. Amplitude Modulation Dynamic Force Microscopy Imaging
938 in Liquids with Atomic Resolution: Comparison of Phase Contrasts in Single and Dual
939 Mode Operation. *Nanotechnology* **2013**, *24* (13), 135702. https://doi.org/10.1088/0957-
940 4484/24/13/135702.
941 (68) Kobayashi, K.; Oyabu, N.; Kimura, K.; Ido, S.; Suzuki, K.; Imai, T.; Tagami, K.;
942 Tsukada, M.; Yamada, H. Visualization of Hydration Layers on Muscovite Mica in
943 Aqueous Solution by Frequency-Modulation Atomic Force Microscopy. *J. Chem. Phys.*
944 **2013**, *138* (18), 184704. https://doi.org/10.1063/1.4803742.
945 (69) Kilpatrick, J. I.; Loh, S. H.; Jarvis, S. P. Directly Probing the Effects of Ions on
946 Hydration Forces at Interfaces. *J. Am. Chem. Soc.* **2013**, *135* (7), 2628–2634.
947 https://doi.org/10.1021/ja310255s.
948 (70) Neumann, J.; Soo Lee, S.; Zhao, E. J.; Fenter, P.; Fenter Julia Neumann, P. Direct
949 Experimental Observations Of Ion Distributions during Overcharging at the Muscovite-
950 Water Interface by Adsorption Of Rb+ And Halides (Cl-, Br-, I-) at High Salinity.
951 *ChemPhysChem* **2023**, e202300545. https://doi.org/10.1002/CPHC.202300545.
952 (71) Iler, R. K. *The Chemistry of Silica. Solubility, Polymerization, Colloid and Surface*
953 *Properties, and Biochemistry*; Wiley: Chichester, United Kingdom, 1979.
954 (72) Liu, J.-F.; Ducker, W. A. Surface-Induced Phase Behavior of Alkyltrimethylammonium
955 Bromide Surfactants Adsorbed to Mica, Silica, and Graphite. *J. Phys. Chem. B* **1999**,
956 *103* (40), 8558–8567. https://doi.org/10.1021/jp991685w.

957 (73) Rashwan, M.; Rehl, B.; Sthoer, A.; Darlington, A. M.; Azam, M. S.; Zeng, H.; Liu, Q.;
958 Tyrode, E.; Gibbs, J. M. Structure of the Silica/Divalent Electrolyte Interface: Molecular
959 Insight into Charge Inversion with Increasing PH. *J. Phys. Chem. C* **2020**, *124* (49),
960 26973–26981. https://doi.org/10.1021/acs.jpcc.0c09747.
961 (74) Zhuravlev, L. T. The Surface Chemistry of Amorphous Silica. Zhuravlev Model.
962 *Colloids Surfaces A Physicochem. Eng. Asp.* **2000**, *173* (1–3), 1–38.
963 https://doi.org/10.1016/S0927-7757(00)00556-2.
964 (75) Goloub, T. P.; Koopal, L. K.; Bijsterbosch, B. H.; Sidorova, M. P. Adsorption of
965 Cationic Surfactants on Silica. Surface Charge Effects. *Langmuir* **1996**, *12* (13), 3188–
966 3194. https://doi.org/10.1021/la9505475.
967 (76) Hashizume, T.; Nakasaki, R.; Ootomo, S.; Oyama, S.; Hasegawa, H. Surface
968 Characterization of GaN and AlGaN Layers Grown by MOVPE. *Mater. Sci. Eng. B*
969 *Solid-State Mater. Adv. Technol.* **2001**, *80* (1–3), 309–312.
970 https://doi.org/10.1016/S0921-5107(00)00647-4.
971 (77) Watkins, N. J.; Wicks, G. W.; Gao, Y. Oxidation Study of GaN Using X-Ray
972 Photoemission Spectroscopy. *Appl. Phys. Lett.* **1999**, *75* (17), 2602–2604.
973 https://doi.org/10.1063/1.125091.
974 (78) Jeon, D. Y.; Kim, K. H.; Park, S. J.; Huh, J. H.; Kim, H. Y.; Yim, C. Y.; Kim, G. T.
975 Enhanced Voltage-Current Characteristics of GaN Nanowires Treated by a Selective
976 Reactive Ion Etching. *Appl. Phys. Lett.* **2006**, *89* (2), 023108.
977 https://doi.org/10.1063/1.2220538.
978 (79) Polo-Garzon, F.; Bao, Z.; Zhang, X.; Huang, W.; Wu, Z. Surface Reconstructions of
979 Metal Oxides and the Consequences on Catalytic Chemistry. *ACS Catalysis*. American
980 Chemical Society June 7, 2019, pp 5692–5707.
981 https://doi.org/10.1021/acscatal.9b01097.

(80) Wang, H.; Zhang, H.; Liu, J.; Xue, D.; Liang, H.; Xia, X. Hydroxyl Group Adsorption on GaN (0001) Surface: First Principles and XPS Studies. *J. Electron. Mater.* **2019**, *48* (4), 2430–2437. https://doi.org/10.1007/s11664-019-07011-1.

(81) Mandal, S.; Thomas, E. L. H.; Middleton, C.; Gines, L.; Griffiths, J. T.; Kappers, M. J.; Oliver, R. A.; Wallis, D. J.; Goff, L. E.; Lynch, S. A.; Kuball, M.; Williams, O. A. Surface Zeta Potential and Diamond Seeding on Gallium Nitride Films. *ACS Omega* **2017**, *2* (10), 7275–7280. https://doi.org/10.1021/acsomega.7b01069.

(82) Wang, J.; Zhang, X.; Wang, C.; Li, H.; Li, H.; Keller, S.; Mishra, U. K.; Nener, B. D.; Parish, G.; Atkin, R. PH-Dependent Surface Properties of the Gallium Nitride – Solution Interface Mapped by Surfactant Adsorption. *J. Colloid Interface Sci.* **2019**, *556*, 680–688. https://doi.org/10.1016/j.jcis.2019.08.079.

(83) Wang, J.; Li, H.; Li, H.; Kellern, S.; Mishra, U. K.; Nener, B. D.; Parish, G.; Atkin, R. Effects of Surface Oxidation on the PH-Dependent Surface Charge of Oxidized Aluminum Gallium Nitride. *J. Colloid Interface Sci.* **2021**, *603*, 604–614. https://doi.org/10.1016/j.jcis.2021.06.126.

(84) Machesky, M. L.; Wesolowski, D. J.; Palmer, D. A.; Ichiro-Hayashi, K. Potentiometric Titrations of Rutile Suspensions to 250°C. *J. Colloid Interface Sci.* **1998**, *200* (2), 298–309. https://doi.org/10.1006/jcis.1997.5401.

(85) Wang, J.; Zhang, X.; Li, H.; Wang, C.; Li, H.; Keller, S.; Mishra, U. K.; Nener, B. D.; Parish, G.; Atkin, R. PH-Dependent Surface Charge at the Interfaces between Aluminum Gallium Nitride (AlGaN) and Aqueous Solution Revealed by Surfactant Adsorption. *J. Colloid Interface Sci.* **2021**, *583*, 331–339. https://doi.org/10.1016/j.jcis.2020.09.036.

(86) Zhang, Z.; Li, X.; Yin, J.; Xu, Y.; Fei, W.; Xue, M.; Wang, Q.; Zhou, J.; Guo, W. Emerging Hydrovoltaic Technology. *Nature Nanotechnology*. Nature Publishing Group December 6, 2018, pp 1109–1119. https://doi.org/10.1038/s41565-018-0228-6.

(87) Mao, X.; Brown, P.; Červinka, C.; Hazell, G.; Li, H.; Ren, Y.; Chen, D.; Atkin, R.; Eastoe, J.; Grillo, I.; Padua, A. A. H.; Costa Gomes, M. F.; Hatton, T. A. Self-Assembled Nanostructures in Ionic Liquids Facilitate Charge Storage at Electrified Interfaces. *Nat. Mater.* **2019**, *18* (12), 1350–1357. https://doi.org/10.1038/s41563-019-0449-6.

(88) Liu, M.; Pang, Y.; Zhang, B.; De Luna, P.; Voznyy, O.; Xu, J.; Zheng, X.; Dinh, C. T.; Fan, F.; Cao, C.; De Arquer, F. P. G.; Safaei, T. S.; Mepham, A.; Klinkova, A.; Kumacheva, E.; Filleter, T.; Sinton, D.; Kelley, S. O.; Sargent, E. H. Enhanced Electrocatalytic CO2 Reduction via Field-Induced Reagent Concentration. *Nature* **2016**, *537* (7620), 382–386. https://doi.org/10.1038/nature19060.

(89) Gilson, M. K.; Honig, B. H. Calculation of Electrostatic Potentials in an Enzyme Active Site. *Nature* **1987**, *330* (6143), 84–86. https://doi.org/10.1038/330084a0.

(90) Shapiro, M. G.; Homma, K.; Villarreal, S.; Richter, C. P.; Bezanilla, F. Infrared Light Excites Cells by Changing Their Electrical Capacitance. *Nat. Commun.* **2012**, *3* (1), 1–11. https://doi.org/10.1038/ncomms1742.

(91) Mann, S.; Heywood, B. R.; Rajam, S.; Birchall, J. D. Controlled Crystallization of CaCO3 under Stearic Acid Monolayers. *Nature* **1988**, *334* (6184), 692–695. https://doi.org/10.1038/334692a0.

(92) Lin, S.; Xu, L.; Chi Wang, A.; Wang, Z. L. Quantifying Electron-Transfer in Liquid-Solid Contact Electrification and the Formation of Electric Double-Layer. *Nat. Commun.* **2020**, *11* (1), 1–8. https://doi.org/10.1038/s41467-019-14278-9.

(93) Shin, S. J.; Kim, D. H.; Bae, G.; Ringe, S.; Choi, H.; Lim, H. K.; Choi, C. H.; Kim, H. On the Importance of the Electric Double Layer Structure in Aqueous Electrocatalysis. *Nat. Commun.* **2022**, *13* (1), 1–8. https://doi.org/10.1038/s41467-021-27909-x.

(94) Garaj, S.; Hubbard, W.; Reina, A.; Kong, J.; Branton, D.; Golovchenko, J. A. Graphene as a Subnanometre Trans-Electrode Membrane. *Nature* **2010**, *467* (7312), 190–193.

https://doi.org/10.1038/nature09379.

(95) Bohra, D.; Chaudhry, J. H.; Burdyny, T.; Pidko, E. A.; Smith, W. A. Modeling the Electrical Double Layer to Understand the Reaction Environment in a CO2 Electrocatalytic System. *Energy Environ. Sci.* **2019**, *12* (11), 3380–3389. https://doi.org/10.1039/c9ee02485a.

(96) Sposito, G. On Points of Zero Charge. *Environ. Sci. Technol.* **1998**, *32* (19), 2815–2819. https://doi.org/10.1021/es9802347.

(97) Nel, A. E.; Mädler, L.; Velegol, D.; Xia, T.; Hoek, E. M. V.; Somasundaran, P.; Klaessig, F.; Castranova, V.; Thompson, M. Understanding Biophysicochemical Interactions at the Nano-Bio Interface. *Nature Materials*. Nature Publishing Group June 14, 2009, pp 543–557. https://doi.org/10.1038/nmat2442.

(98) Ji, H.; Zhao, X.; Qiao, Z.; Jung, J.; Zhu, Y.; Lu, Y.; Zhang, L. L.; MacDonald, A. H.; Ruoff, R. S. Capacitance of Carbon-Based Electrical Double-Layer Capacitors. *Nat. Commun.* **2014**, *5* (1), 1–7. https://doi.org/10.1038/ncomms4317.

(99) Wallentine, S.; Bandaranayake, S.; Biswas, S.; Baker, L. R. Direct Observation of Carbon Dioxide Electroreduction on Gold: Site Blocking by the Stern Layer Controls CO2Adsorption Kinetics. *J. Phys. Chem. Lett.* **2020**, *11* (19), 8307–8313. https://doi.org/10.1021/acs.jpclett.0c02628.

(100) Liu, N.; Chen, R.; Wan, Q. Recent Advances in Electric-Double-Layer Transistors for Bio-Chemical Sensing Applications. *Sensors (Switzerland)*. Multidisciplinary Digital Publishing Institute August 5, 2019, p 3425. https://doi.org/10.3390/s19153425.

(101) Hutter, J. L.; Bechhoefer, J. Calibration of Atomic-Force Microscope Tips. *Rev. Sci. Instrum.* **1993**, *64* (7), 1868–1873. https://doi.org/10.1063/1.1143970.

Supporting Information for

Ions Adsorbed at Amorphous Solid / Solution Interfaces Form Wigner Crystal-Like Structures

Jianan Wang,[1] Hua Li,[1,2] Mahdi Tavakol,[3] Alessandra Serva,[4] Brett Nener,[5] Giacinta Parish,[5] Mathieu Salanne,[4] Gregory G. Warr,[6] Kislon Voïtchovsky,[5] Rob Atkin[1*]

[1]School of Molecular Sciences, The University of Western Australia, Perth, 6009, Australia

[2]Centre for Microscopy, Characterisation and Analysis, The University of Western Australia, Perth, 6009, Australia

[3]Department of Physics, Durham University, Durham, DH1 3LE, UK

[4]Sorbonne Université, CNRS, Physicochimie des Électrolytes et Nanosystèmes Interfaciaux, PHENIX, Paris, F-75005, France

[5]School of Engineering, The University of Western Australia, Perth, 6009, Australia

[6]School of Chemistry and Sydney Nano Institute, The University of Sydney, Sydney, 2006, Australia

*E-mail: rob.atkin@uwa.edu.au

Supplementary Notes

Supplementary Note 1. Simulation Details

Two types of molecular dynamics (MD) simulations were conducted to explore the underlying mechanism of ionic cluster formation and confirm the experimental findings.

a. *MD simulations with non-polarizable force field*

First, two (111) gold facets with lateral dimensions of 6 nm × 6 nm and thickness of ~ 1.4 nm were placed ~ 8 nm apart (see Fig. S16). 9000 flexible SPC water molecules (SPC/Fw)[1] were then added to the simulation box in such a way so that half of them occupy the region between the plates. The Mg^{2+} and Cl^- ions required to reach specific $MgCl_2$ concentration were then added to the simulation box with the same number of ions inside and outside the region between plates (Fig. S16). Interactions between gold atoms and water were calculated through the non-polarizable interface forcefield parameters for gold[2]. After an energy minimization of several hundred steps, several short equilibration runs of 1000 steps were conducted under the NPT ensemble to reach an equilibrated water density and eliminate large variations along the length of the simulation. Then, the main equilibration sequence was conducted, consisting of a 10 ns simulation, prior to the main simulation where electric potentials are applied. The potential was imposed between the gold plates as a constant (DC) electric field (see Fig. S16). Each time step of the equilibration and simulation represents 1 fs. All the simulations were carried out at temperature and pressure of 310 K and 1 atm respectively employing a Nose-Hoover thermostat and barostat. The long-range electrostatic interactions were calculated through the PPPM method with an energy tolerance of 1e-4 [3]. Some control simulations were run for 200 ns after the equilibration phase to ensure minimal evolution of the system with the results showing the formation of clusters as large as 20 ions at the interface in the expense of the number of smaller clusters. All the analysis was conducted with bespoke python routines

(freely available on GitHub[4]) aimed as quantifying ionic clusters at the interface and in the bulk liquid. Two adjacent ions were counted as part of a same cluster if their center-to-center distance is less than 4.147 Å, 35% more than the van der Waals radius for Mg-Cl interactions. The distinction between interfacial and bulk clusters was achieved using a threshold distance from the gold surface: any clusters with at least one ion within 5.5 Å of the surface was counted as interfacial. The threshold of 5.5 Å was chosen based on the location of first peaks for Mg^{2+} and Cl^- layers under 4 V (see Fig. S3a). The details of each simulation including the number of atoms, number of ions, number of water molecules, average $MgCl_2$ concentration, applied voltage and length of simulation are summarized in the Table S1.

Table S1. Details of the simulations done in the current study.

$MgCl_2$ concentration	Mg^{2+}	Cl^-	Electric field (mV/A)	Gold voltage (V)	Simulation time (ns)	Number of simulations	Total time (ns)
2.85 (M)	462	924	0	0	10	3	30
			25.54	2	10	3	30
			51.09	4	10	3	30
			255.43	20	10	3	30
			51.09	4	210	1	210
0.71M	116	232	0	0	10	3	30
			51.09	4	10	3	30
			255.43	20	10	3	30
1.425M	230	460	51.09	4	10	3	30
0.175M	30	60	51.09	4	10	3	30
Accumulated simulation time (ns)							480

b. *MD simulations with fluctuating changes on the gold surface*

Classical MD simulations at a fixed potential difference of 0, 1, 2, and 4 V were performed with the MetalWalls code[5]. The system was made of 9000 H_2O molecules, 462 Mg^{2+} ions and 924 Cl^- ions in between two Au(111) electrodes, each with 3528 atoms distributed in 7 planes. A representative snapshot of the system is shown in Fig. S17. The force field parameters were the same as the ones used for the MD simulations with non-polarizable force field. In addition to the Lennard-Jones, gold atoms were modelled using Gaussian charge distributions, with Gaussian width of 1.17 Å according to [6].

The system was simulated in the NVT ensemble with a timestep of 1 fs, for a total of 13 ns. The Nosé-Hoover thermostat chain was used with a time constant of 0.5 ps to maintain a temperature of 298 K. 2D periodic boundary conditions were employed, with no periodicity on the direction normal to the Au surface. The electrode charges were calculated at each time step using a matrix inversion method to enforce both the constant applied potential between the two electrodes and the electroneutrality constraints on the charges. The first 3 ns (until the total charge on the electrode reaches a plateau, as shown in Fig. S17) were considered as equilibration, followed by 10 ns production.

Supplementary Note 2. AFM phase and topography images

In this study, AFM phase images and topographical images are used to show adsorbed ions, as is a common practice for similar studies presenting high-resolution AM-AFM images[7–10]. In particular, phase images show the subtle changes in the compliance of the imaged surface[11]: dark and bright spots on a phase image indicate relatively compliant and non-compliant spots on the surface, respectively. Occasionally, the atoms on sample surfaces and the surface-adsorbed ions may not differ significantly in height due to the small scale of atoms/ions, but the surface and the ions may present different mechanical properties which can cause a phase shift for the AFM tip, and ion adsorption can then be uncovered in the phase images. Therefore, phase images are shown in the main article below, while topography images are included as supplementary figures to support the phase images. For the systems imaged in this study, scan sizes of both 5 nm × 5 nm and 10 nm × 10 nm were captured. Images of one size are presented in the main article below and images of the other scan size are presented as supplementary figures. The images features scale correctly to the scan size, suggesting that the features are real and not artifacts or noise.

Supplementary Note 3. AFM images acquired with different AFM probes and different solvents

To further confirm the reproducibility of the AFM results and exclude the effect of AFM tips on the results, Figs. S8–S11 compare AFM images of Stern layers acquired with AFM tips with different coatings (silica and diamond) for various ions on gold and silica surfaces. Also, Fig. S12 presents AFM images of the Stern layers at gold/KCl solutions interfaces with water or dimethyl sulfoxide (DMSO) as the solvent. Only gold surfaces were used to avoid the complex determination of solution pH with a non-water solvent. The images features are in broad agreement when different tips or solvents are used. That is, the crystallinity of Stern layers is retained at high ion concentrations and high surface charge. There are subtle differences between images acquired in water and in DMSO due to the different ion hydration states. This will be explained further in Supplementary Note 4.

Supplementary Note 4. Role of solvent in ion adsorption

As discussed in the main article, a hydration network may facilitate ordered ion adsorption[10]. To further explore this mechanism, we conducted a set of experiments comparing the adsorption of a moderate concentration of K^+ in different solvents, namely water and dimethyl sulfoxide (DMSO), to a gold surface with adjustable surface potential (see Methods). Fig. S12 presents the results.

At open-circuit potential (OCP), a negligible number of K^+ ions from the aqueous solution adsorb to the gold surface, as evidenced by the almost featureless image of the surface. In contrast, in DMSO, despite a slightly lower ion concentration, spherical features corresponding to adsorbed K^+ ions can be observed. The features (0.5 – 0.8 nm in diameter) may seem very large for K^+ ions (0.3 nm in diameter for bare ions[12]). This is most likely due to the low magnitude of surface potential causing a weak electrostatic attraction which in turn means the adsorbed ions can move relatively freely. In the case of aqueous solution, the K^+ ions may adsorb as hydrated ions, whose size (0.66 nm in diameter[13]) is comparable to the image features. The AFM tip, which is relatively slow compared to the ion movement, captures the average position of the ions[14], so the imaged ions appear larger than the real ion size. The difference between the adsorption features for the aqueous solution and the DMSO solution is most likely resulted from the different hydration statuses for the K^+ ions. In the aqueous solution, the K^+ ions are hydrated, and the loosely adsorbed hydrated ions are easily displaced by the AFM tip. In comparison, without a hydration shell in the DMSO solution, the K^+ ions are able to be closer to the surface and be more strongly attracted to the surface, and thus less likely to be displaced by the AFM tip.

When the surface is negatively biased, attracting a significant number of K^+ ions, however, the adsorbed K^+ ions appear clearer and more densely packed in the aqueous solution than in DMSO. This indicates that the ion adsorption is stronger in the aqueous solution at this negative surface potential.

The difference in the relative amount of ion adsorption at different surface potentials may seem surprising at first glance, considering the hydration status of the individual ions in both solvents remain mostly unchanged: K^+ ions are mostly likely adsorbed to the surface in an outer-sphere configuration in the aqueous solution and without a hydration shell in DMSO. Therefore, there must be more influencing factors. And the greater surface excess increase in the aqueous solution than in DMSO with increasing surface potential magnitude is most likely to be caused by the different global hydration landscapes for the two solvents. The DMSO is aprotic and lacks a bulk structure such as a hydrogen bond network. As a result, the dehydrated K^+ ions adsorb to the gold surface almost *via* electrostatic attractions alone, and there is negligible solvent-mediated correlation of the surface adsorbed ions. On the contrary, in the aqueous solution, water molecules can drive a more attractive correlation between neighboring ions, and hence a hydration network can stabilize more ions at the same surface potential[10], causing a higher surface excess with a significant amount of initial ion adsorption.

Supplementary Note 5. Surface excess and percentage by volume of adsorbed ions

To characterize the ion adsorption more quantitively, the surface excess and percentage by volume for the adsorbed ions were calculated. Unlike highly smooth surfaces commonly used for AFM studies such as mica and calcite, GaN and silica surfaces are not atomically flat. As a result, determining adsorbed ions on an image with undulating surface structures is difficult. To address this issue, for the calculation of surface excess of ions, three 2 nm^2 square-shaped regions with relatively small height variation and clear surface features are chosen for each liquid system, and the adsorbed ions in the areas are counted as a representation of ion adsorption on the whole surface. In Figs. S9 and S10, adsorbed ions are marked using red circles with size corresponding to the dehydrated ion size. The bright features are counted as adsorbed ions because they are consistent with the bright (raised) features in the height images (Figs. S1–S5), and the feature sizes broadly match the diameters of dehydrated ions. Only globular features that can fill a circle are counted as adsorbed ions. Imperfect features are unlikely to be the result of ion adsorption, since the images presented in this study are the representative images with the best imaging quality among tens of images acquired across different experiment days. For example, the ion counts within the three selected 2 nm^2 areas in Fig. S9(a) are 4, 4 and 5, respectively. This method may result in a slight overestimation of the surface excess, because surface regions with no ion adsorption due to a lack of charged sites and/or surface hydrophobicity may be underrepresented in the selected areas. However, this potential error is minimized through averaging the results for the three different regions. Therefore, the surface excess values deduced from the AFM images here should serve as a good indication of the surface charge and the density of surface-adsorbed ions. The values of ion count per 2 nm^2 are converted to surface excess values. For example, for an ion count per 2 nm^2 area of 9:

$$\text{surface excess} = \text{ion count}/\text{nm}^2 \times \frac{1}{N_A}$$

$$= 9/2\ \text{nm}^{-2} \times \frac{1}{6.02 \times 10^{23}\ /\text{mol}} \times \frac{(10^9)^2\ \text{nm}^2}{\text{m}^2} \times \frac{10^6\ \mu\text{mol}}{\text{mol}}$$

$$= 7.5\ \mu\text{mol}/\text{m}^2$$

Table S2 summarizes the calculation results. The results show that as the ion concentration increases exponentially, the surface excess of adsorbed ions also increases exponentially, but by a different factor. For example, for GaN, at pH 10, when the $CaCl_2$ concentration increases from 1 mM to 10 mM and from 10 mM to 100 mM, the surface excess of adsorbed Ca^{2+} ions increases by 1.32 and 1.38 times, respectively. This trend is consistent with previous reported surface excess data measured with potentiometric titrations[15]. The result also shows that when the pH is reduced from 10 to 9, thus reducing the negative surface charge, the surface excess of adsorbed K^+ ions decreases significantly by ~ 40%.

Table S2. Summary of quantitative analysis of images for GaN and silica.

Surface	Solution	pH	Ionic strength /M	Imaged ions	Surface excess /(μmol/m^2)	Ion diameter/nm
GaN	10 mM KCl + 0.1 mM NaOH	10	0.010	K^+	3.6 ± 0.5	0.30
	100 mM KCl + 0.1 mM NaOH	10	0.10		6.9 ± 1.0	
	100 mM KCl + 0.01 mM NaOH	9	0.10		4.2 ± 0.8	
	1 mM $CaCl_2$ + 0.1 mM NaOH	10	0.0030	Ca^{2+}	4.4 ± 0.5	0.23
	10 mM $CaCl_2$ + 0.1 mM NaOH	10	0.030		5.8 ± 0.8	

	100 mM $CaCl_2$ + 0.1 mM NaOH	10	0.30		8.0 ± 0.5	
	100 mM KCl + 10 mM HCl	2	0.11	Cl^-	3.6 ± 0.5	0.36
	95 mM Na_2SO_4 + 5 mM H_2SO_4	2	0.30	SO_4^{2-}	2.8 ± 0.5	0.48
silica	0.10 M KCl+ NaOH	9	0.10		3.3 ± 0.8	
	0.20 M KCl+ NaOH	9	0.20	K^+	4.2	0.30
	1.0 M KCl+ NaOH	9	1.0		4.7 ± 1.0	
	0.10 M $CaCl_2$ + NaOH	9	0.30		5.0 ± 0.8	
	0.38 M $CaCl_2$ + NaOH	9	1.14	Ca^{2+}	6.6 ± 1.7	0.23

For the systems showing crystalline ion adsorption, their bulk solution concentrations may seem surprisingly low for causing such ordered ion adsorption, but as counterions are concentrated near the surface in an electrical double layer[16], the concentration of the adsorbed ions in the Stern layer is significantly higher than in the bulk solution.

This effect of ion valency on the surface excess is also reflected by anion adsorption. The surface excess of SO_4^{2-} is only slightly lower than Cl^- (Table S1). However, Cl^- is monovalent, while SO_4^{2-} is divalent. More accurately, in 5 mM H_2SO_4 + 95 mM Na_2SO_4, HSO_4^- behaves as a weak acid, and all the H^+ ions should be bound with either the GaN surface or SO_4^{2-} ions under the experimental condition[17]. As a result, on average, each SO_4^{2-} ion carries at least 1.9 elementary charges for this system. Therefore, the result indicates that at the same pH, more negative charges adsorb to the GaN surface from divalent SO_4^{2-} than from monovalent Cl^-,

meaning that there is a stronger attraction between the GaN surface and SO_4^{2-} ions at the same pH and similar anion concentrations.

Similar to GaN, the surface excess of adsorbed ions increases with increasing ion concentration for both K^+ and Ca^{2+} (Table S2). However, this increase is not linear, likely because the surface is almost fully neutralized by counterions at such high solution concentrations.

Supplementary Figures

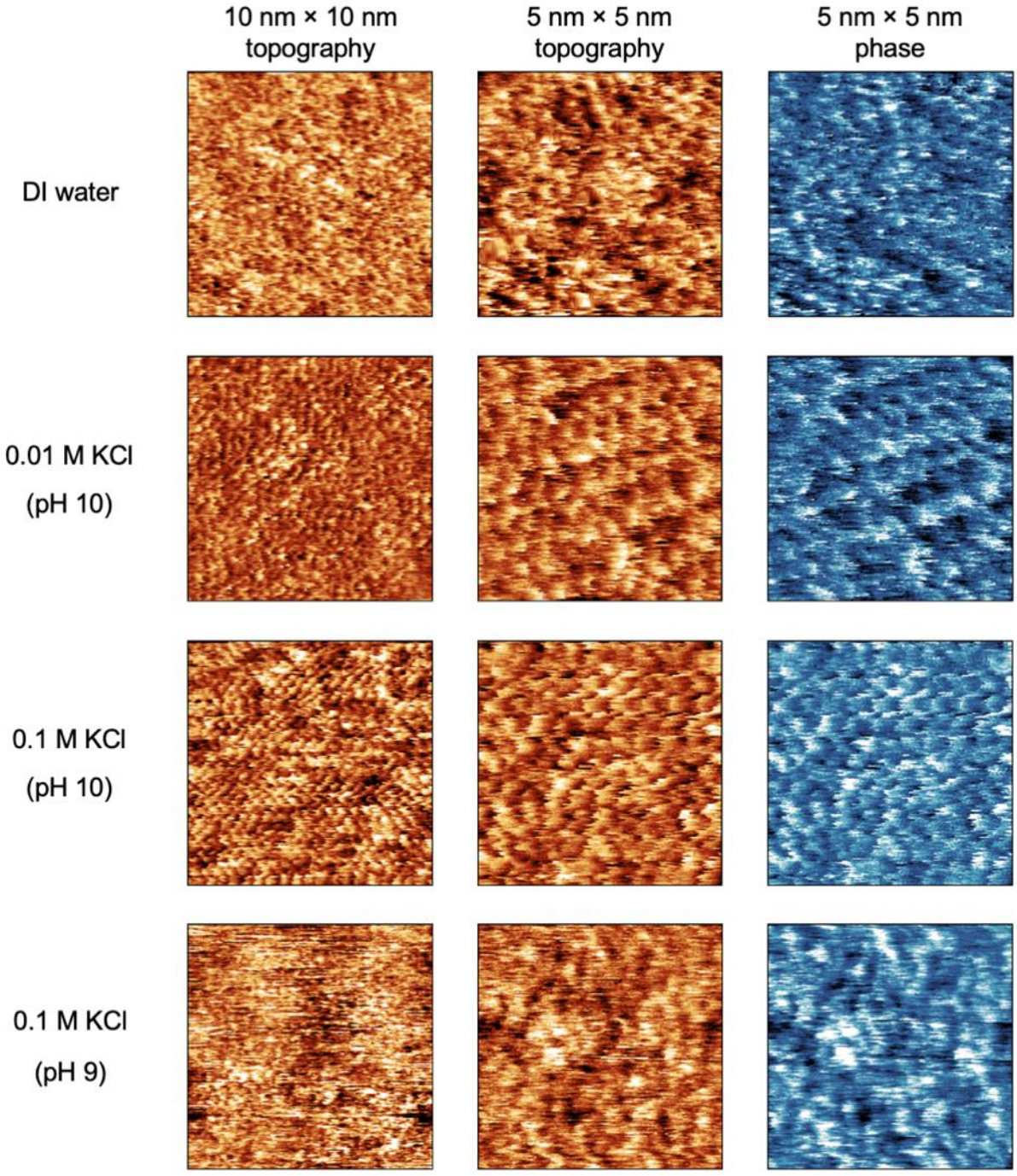

Fig. S1. AFM topography and phase images of the interfaces between a gallium nitride (GaN) surface and various liquid systems as labelled. The deionized (DI) water was saturated with CO_2 and has a pH of ~ 5.5. NaOH was used to adjust solution pH.

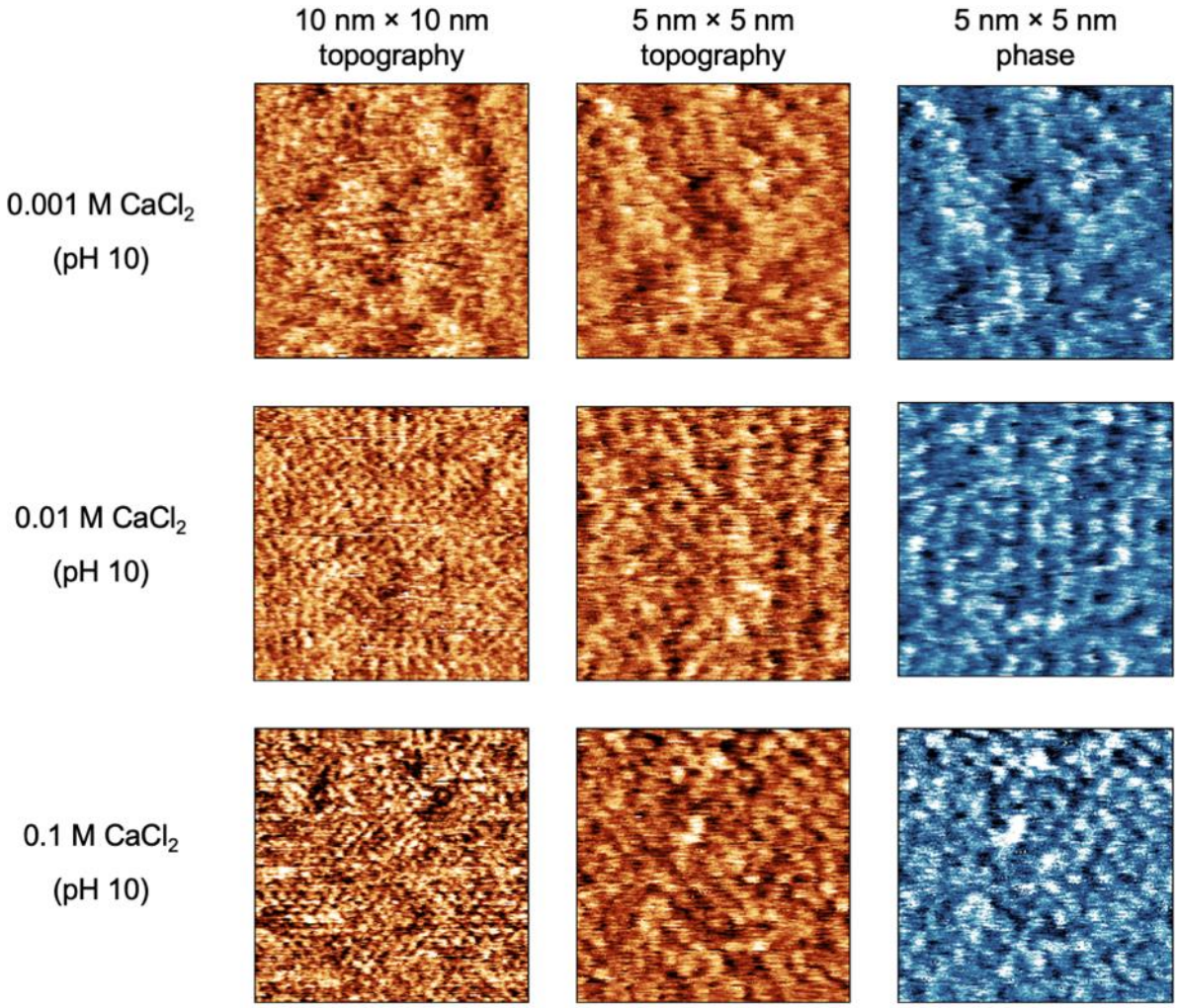

Fig. S2. AFM topography and phase images of the interfaces between a gallium nitride (GaN) surface and $CaCl_2$ solutions at different concentrations as labelled. NaOH was used to adjust solution pH.

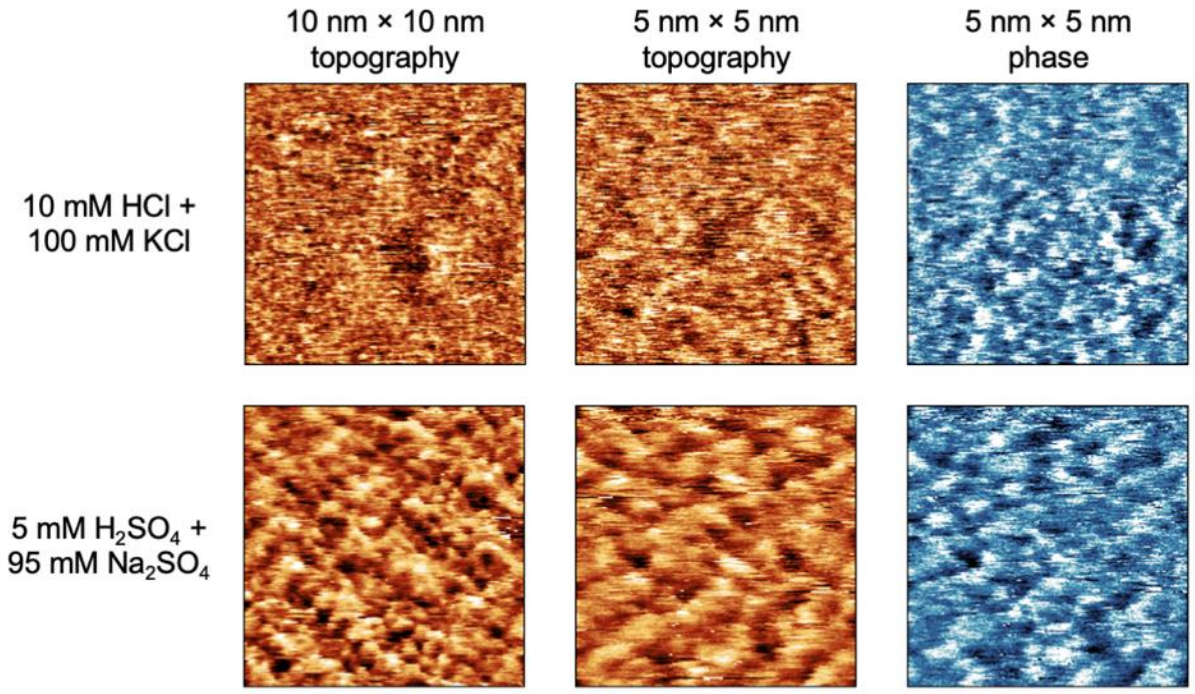

Fig. S3. AFM topography and phase images of the interfaces between a GaN surface and two liquid systems showing anion adsorption as labelled.

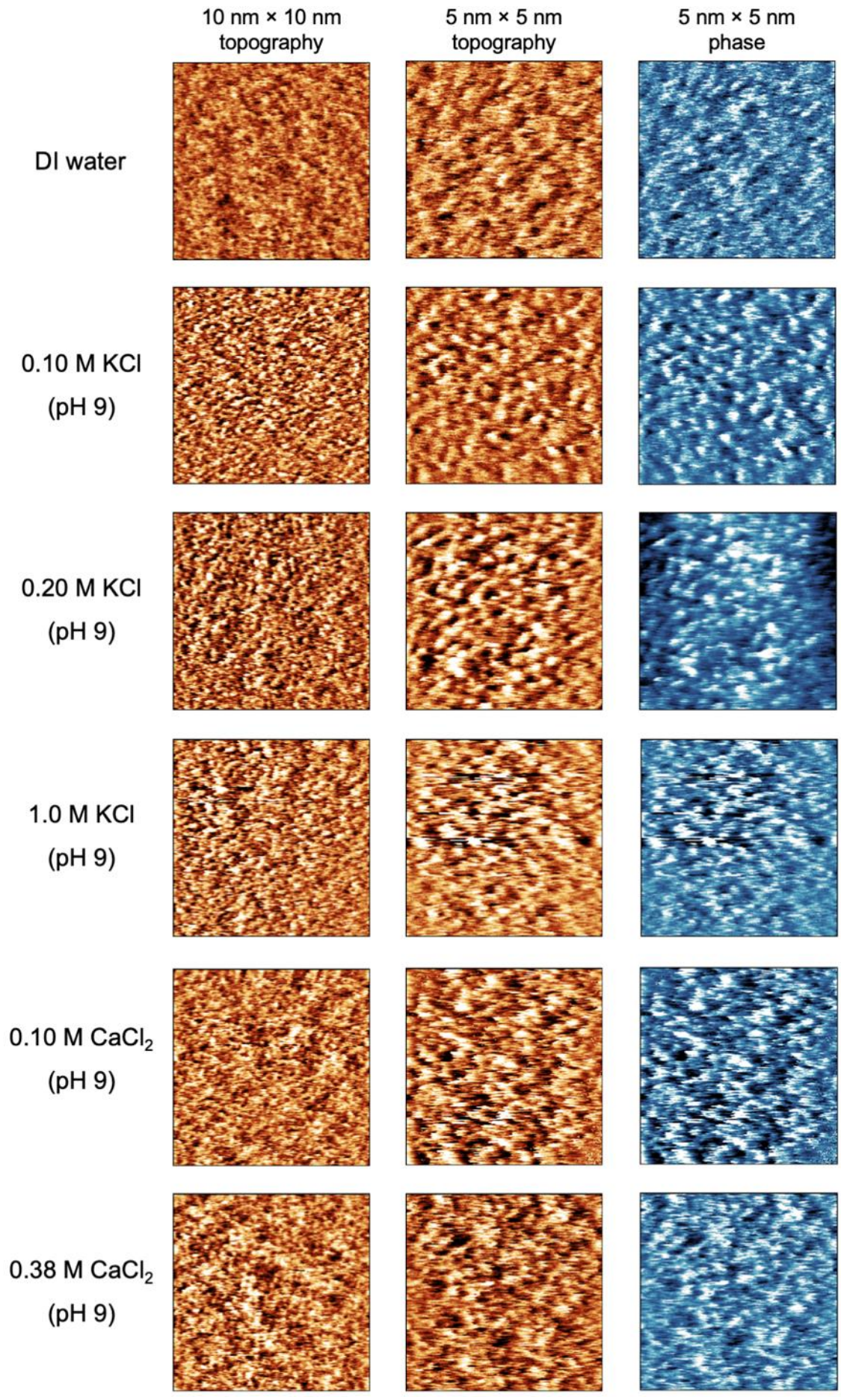
10 nm × 10 nm topography
5 nm × 5 nm topography
5 nm × 5 nm phase
DI water
0.10 M KCl (pH 9)
0.20 M KCl (pH 9)
1.0 M KCl (pH 9)
0.10 M CaCl2 (pH 9)
0.38 M CaCl2 (pH 9)

Fig. S4. AFM topography and phase images of the interfaces between a silica surface and various liquid systems as labelled. The deionized (DI) water was saturated with CO_2 and has a pH of ~ 5.5. NaOH was used to adjust solution pH.

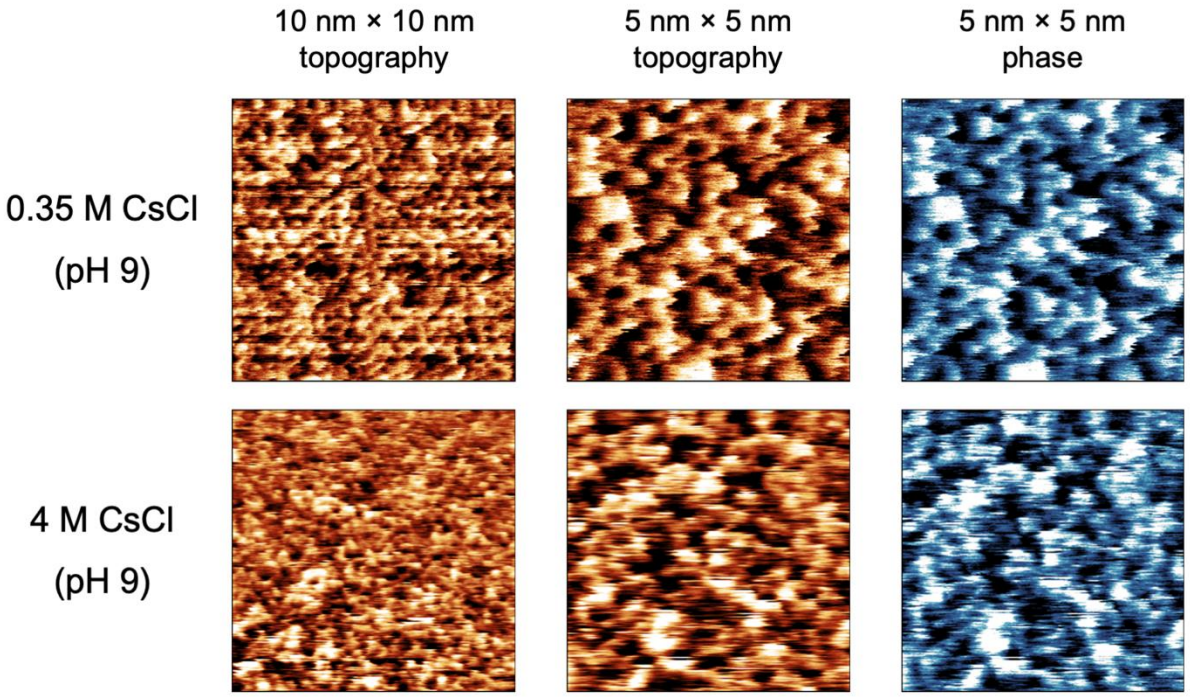

Fig. S5. AFM topography and phase images of the interfaces between a silica surface and 0.35 M as well as 4 M systems as labelled. The deionized (DI) water was saturated with CO_2 and has a pH of ~ 5.5. NaOH was used to adjust solution pH.

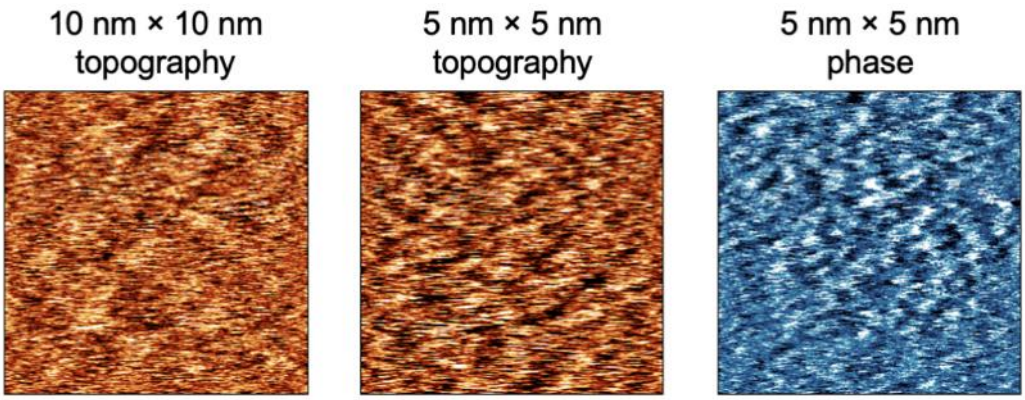

Fig. S6. AFM topography and phase images of the interfaces between a gold surface and deionized (DI) water as labelled. The DI water was saturated with CO_2 and has a pH of ~ 5.5.

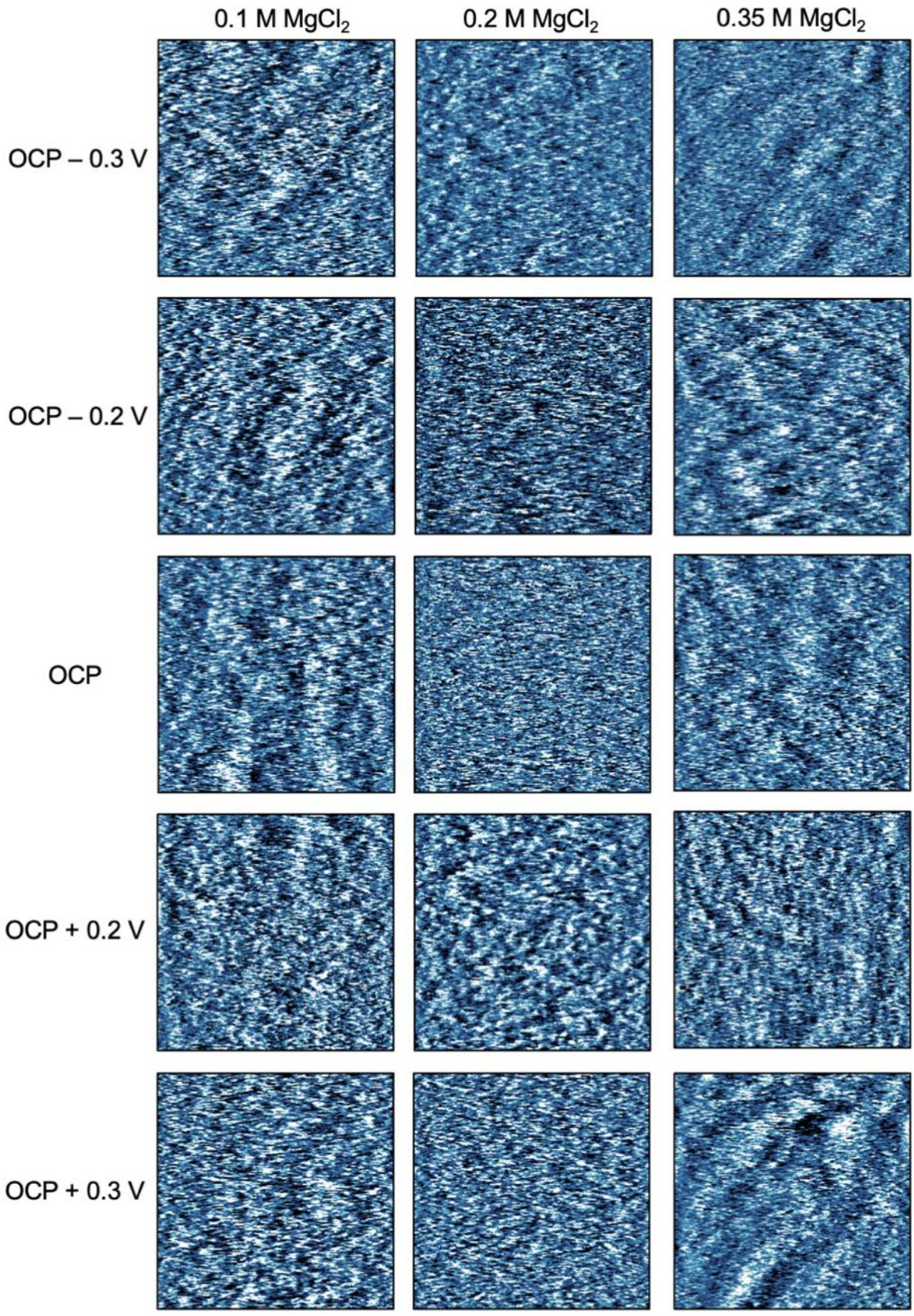
0.1 M MgCl2
0.2 M MgCl2
0.35 M MgCl2
OCP – 0.3 V
OCP – 0.2 V
OCP
OCP + 0.2 V
OCP + 0.3 V

Fig. S7. 10 nm × 10 nm AFM phase images of the interfaces between a gold surface and $MgCl_2$ solutions at various concentrations as labelled. No acids or bases were added to the $MgCl_2$ solutions to adjust the solution pH. OCP: open circuit potential.

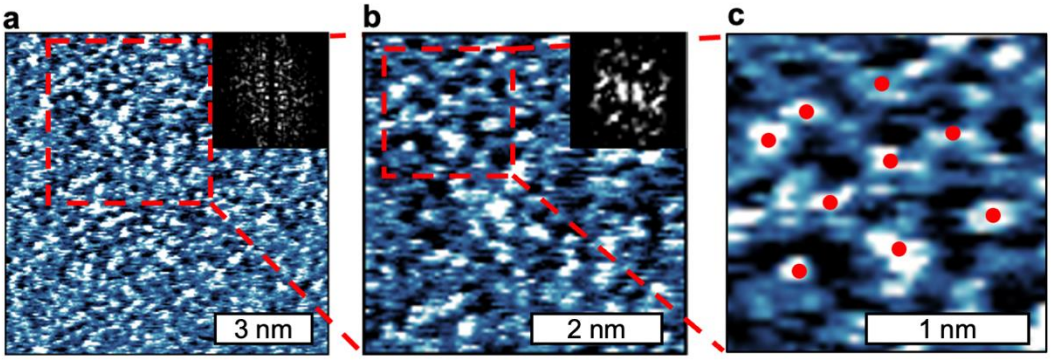

Fig. S8. AFM phase images of the interface between silica and 0.1 M KCl. Insets: 2D-FFT images of the corresponding images. Red dots in the 2 nm × 2 nm images show features partially aligned in a hexagonal structure.

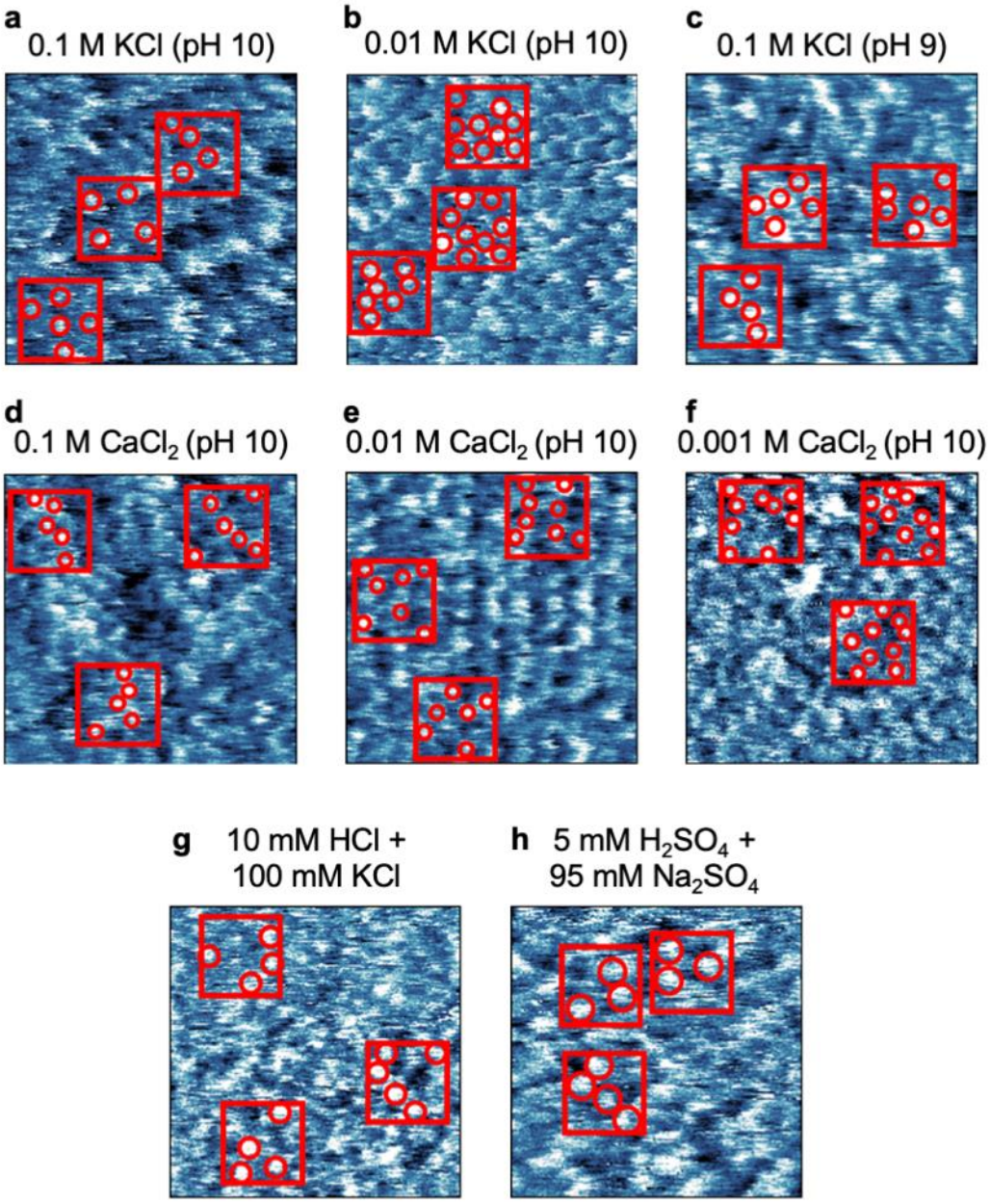

Fig. S9. 5 nm × 5 nm AFM images of the interfaces between a gallium nitride (GaN) surface and various liquid systems as labelled. The red squares correspond to the 2 nm^2 regions where adsorbed ions are counted. The red circles indicate adsorbed ions, and the circle sizes are scaled according to the diameters of dehydrated ions.

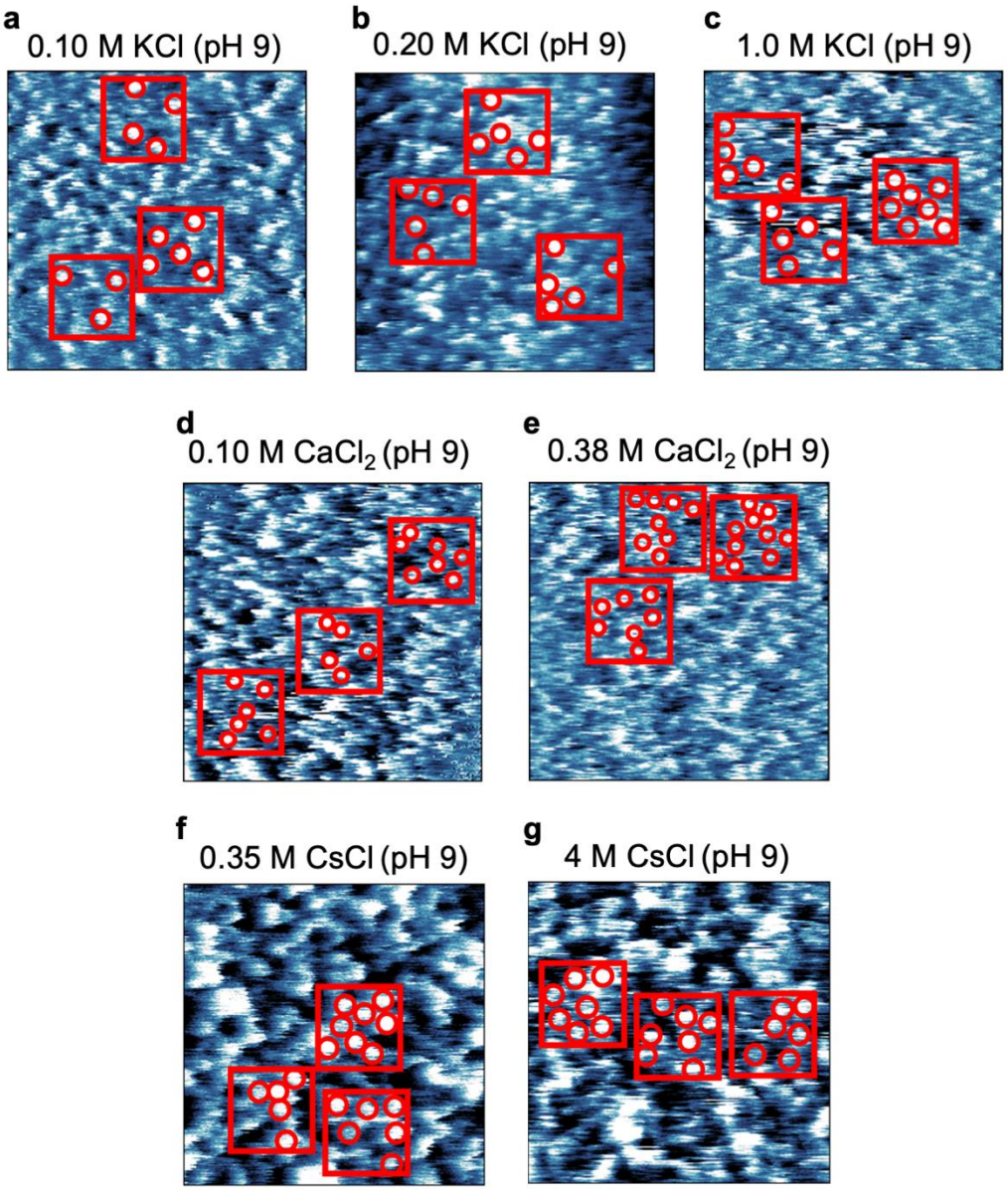

Fig. S10. 5 nm × 5 nm AFM images of the interfaces between a silica surface and various liquid systems as labelled. The red squares correspond to the 2 nm^2 regions where adsorbed ions are counted. The red circles indicate adsorbed ions, and the circle sizes are scaled according to the diameters of dehydrated ions.

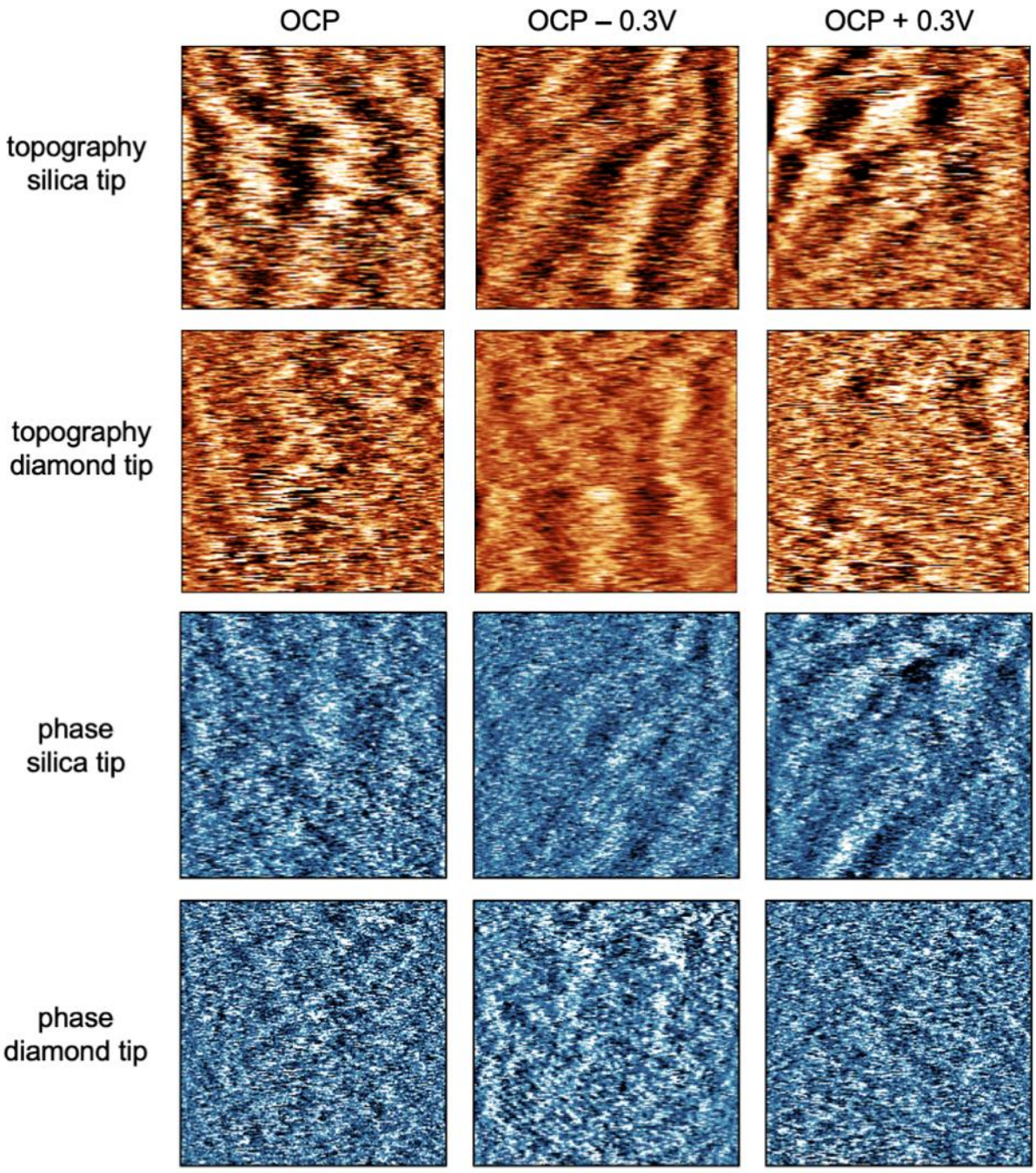

Fig. S11. 10 nm × 10 nm AFM images of the interfaces between a gold surface and 0.35 M $MgCl_2$ at various surface potentials captured using a silica AFM tip (Asylum Research FS-1500) and a diamond tip (Adama Super Sharp) as labelled. No acids or bases were added to the $MgCl_2$ solution to adjust the solution pH. OCP: open circuit potential.

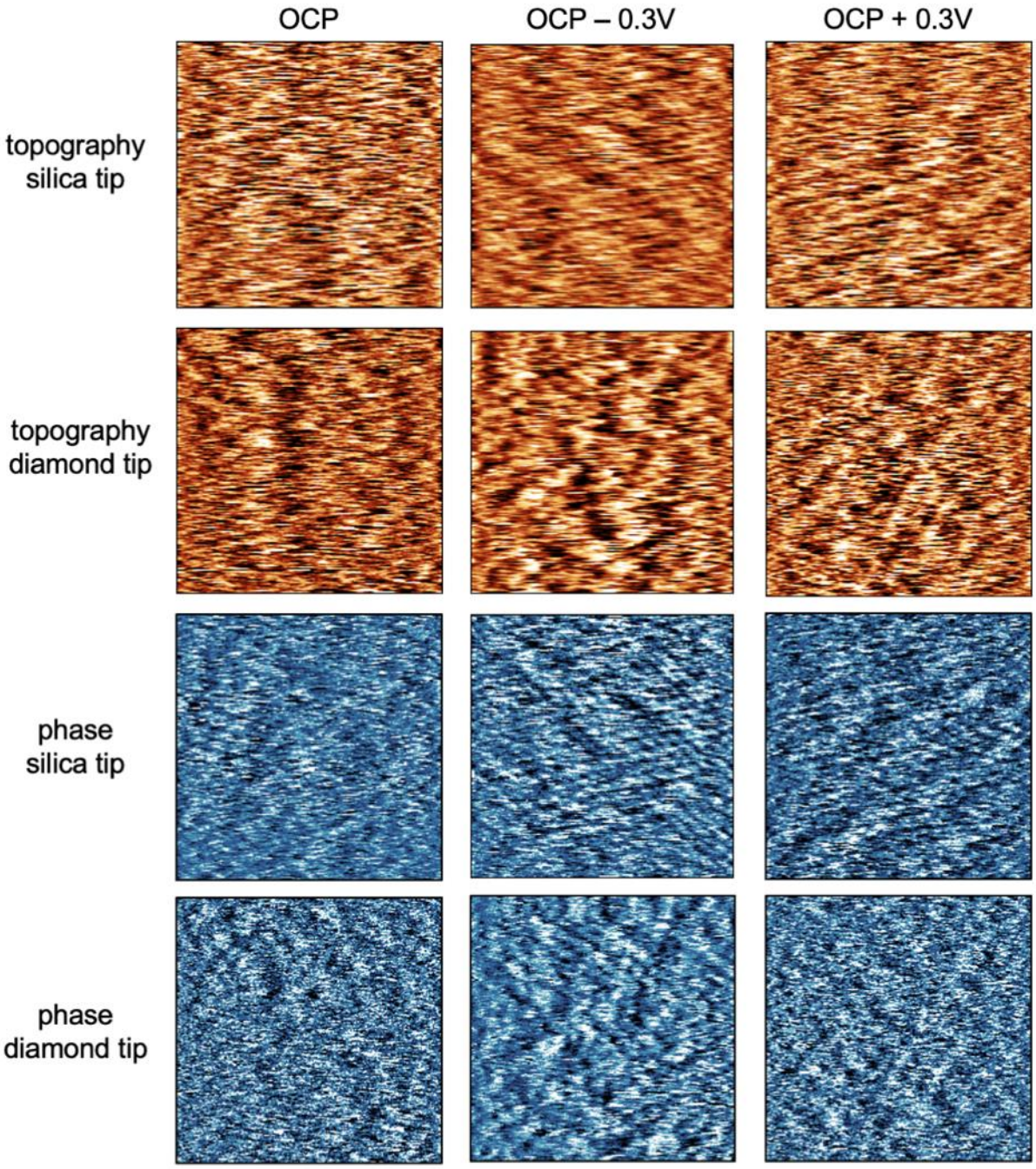

Fig. S12. 5 nm × 5 nm AFM images of the interfaces between a gold surface and 0.35 M $MgCl_2$ at various surface potentials captured using a silica AFM tip (Asylum Research FS-1500) and a diamond tip (Adama Super Sharp) as labelled. No acids or bases were added to the $MgCl_2$ solution to adjust the solution pH. OCP: open circuit potential.

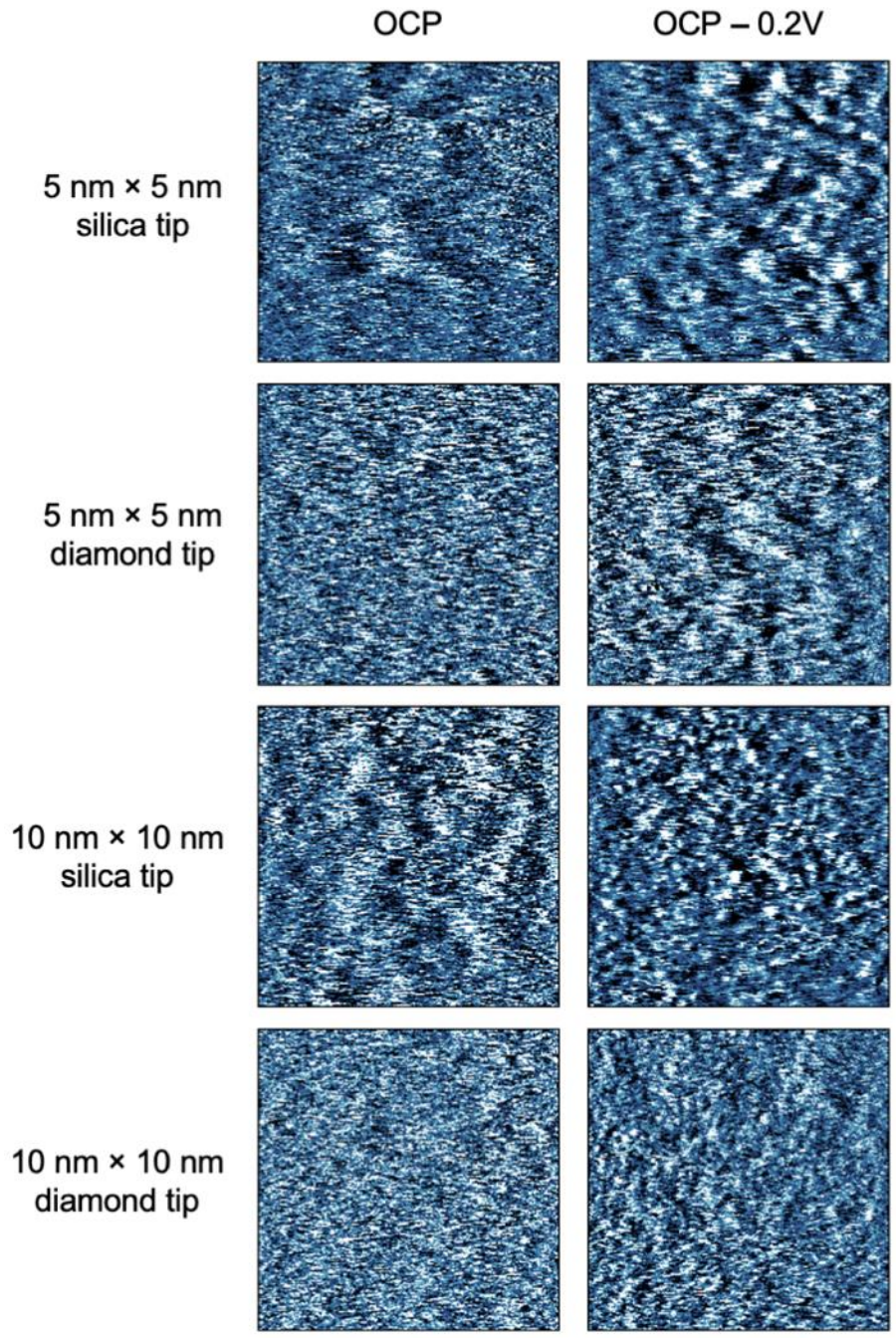

Fig. S13. 5 nm × 5 nm and 10 nm × 10 nm AFM phase images of the interfaces between a gold surface and 1.0 M CsCl aqueous solution at various surface potentials captured using a silica AFM tip (Asylum Research FS-1500) and a diamond tip (Adama Super Sharp) as labelled. No acids or bases were added to the KCl solution to adjust the solution pH. OCP: open circuit potential.

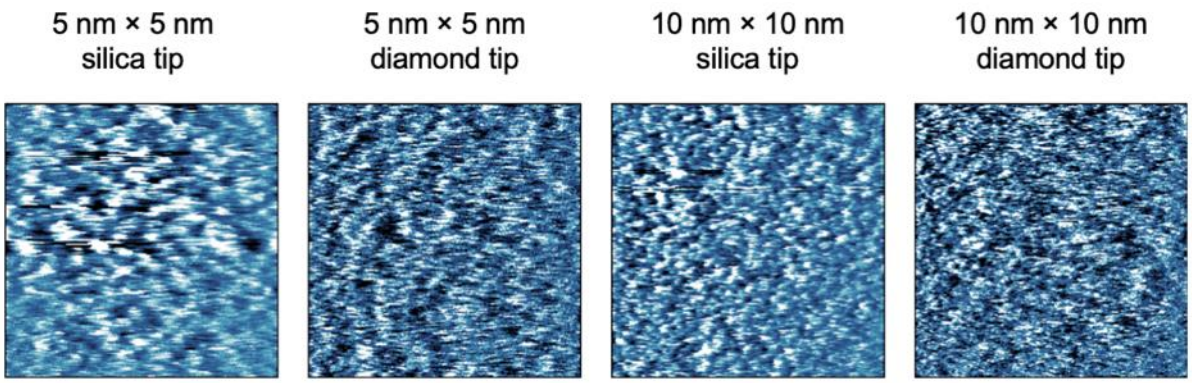

Fig. S14. 5 nm × 5 nm and 10 nm × 10 nm AFM phase images of the interfaces between a silica surface and 1.0 M KCl at pH 9 (NaOH) captured using a silica AFM tip (Asylum Research FS-1500) and a diamond tip (Adama Super Sharp) as labelled.

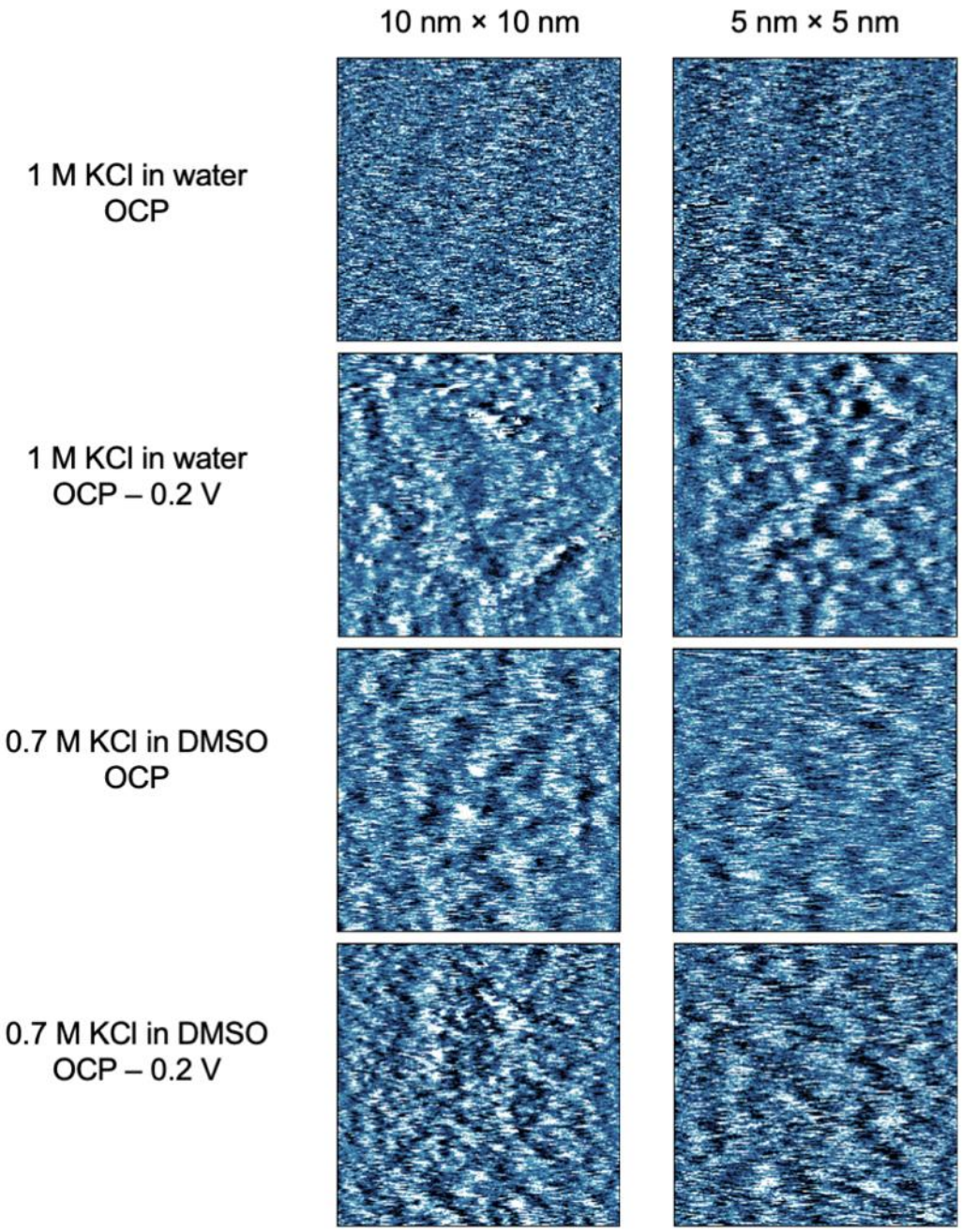

Fig. S15. 5 nm × 5 nm and 10 nm × 10 nm AFM phase images of the interfaces between a gold surface and KCl dissolved in water and DMSO at various surface potentials captured using a silica AFM tip (Asylum Research FS-1500) as labelled. No acids or bases were added to the KCl solution to adjust the solution pH. OCP: open circuit potential.

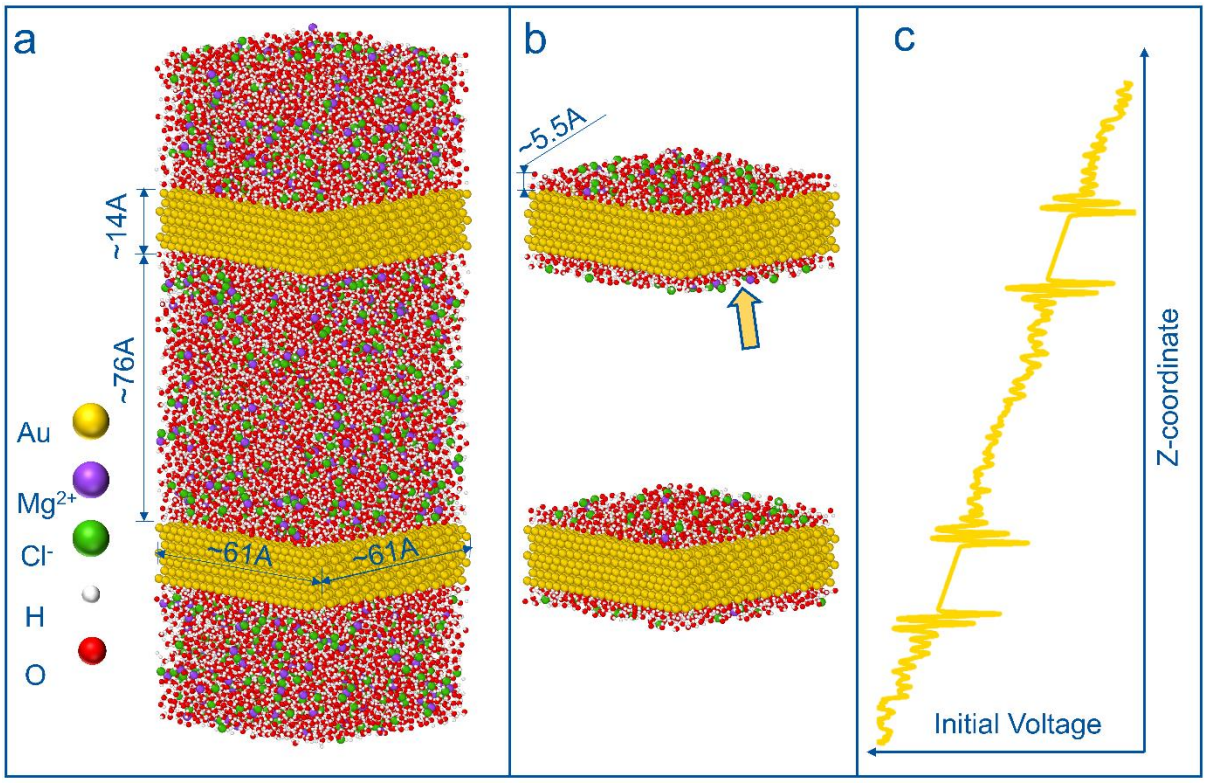

Fig. S16. Details of the simulation setup: (a) the simulation box containing two gold plates and various concentrations of $MgCl_2$ solvated in SPC/Fw water molecules; (b) the interfacial region defined as 5.5 Å above and beneath each gold plate with the arrow indicating the gold surface from which the snapshots were taken for Fig. 3; (c) voltage (when applied to the system) vs. Z-coordinate profile.

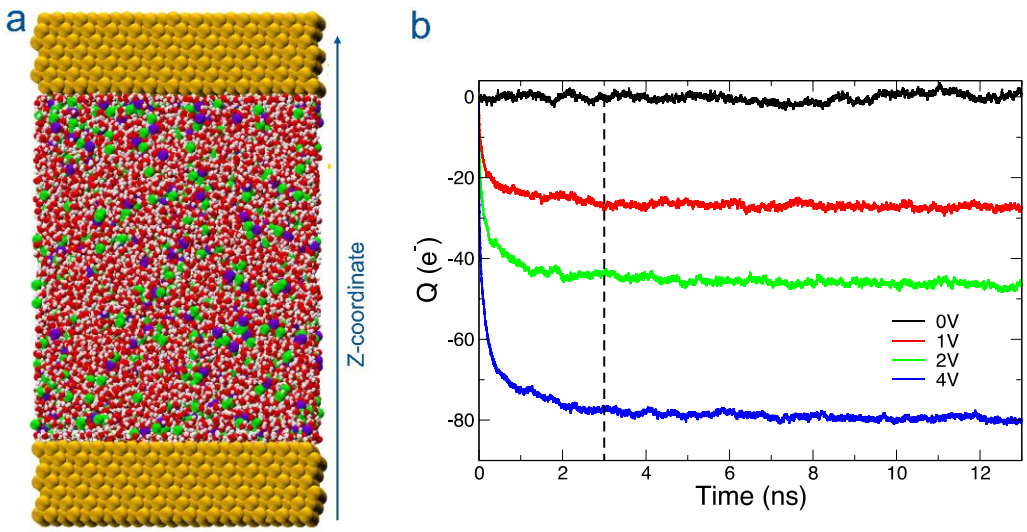

Fig. S17. Details of the setup for the MD simulations with fluctuating charges in the gold electrodes: (a) the simulation box containing two gold plates and a 2.87 M $MgCl_2$ solution (SPC/F used for water molecules); (b) time evolution of the total charge on the negative electrode for an applied potential difference of 0 V (black), 1 V (red), 2 V (green) and 4 V (blue).

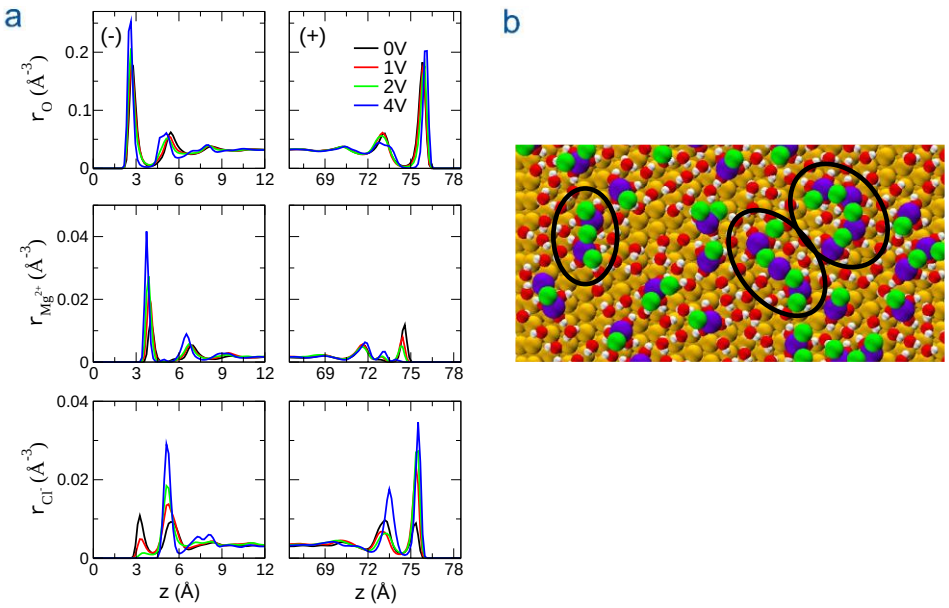

Fig. S18. Computer simulations with fluctuating charges in the gold surface for the 2.85 M $MgCl_2$ solution (see Supplementary Note 1). (a) Density profiles in the direction perpendicular to the electrode (vertical coordinate z) for various applied voltage: water (top), Mg^{2+} ions (middle) and Cl^- (bottom). Negative and positive electrodes are shown in the left and right panels, respectively. (b) MD snapshot for the 4V simulation, with Mg^{2+} ions in purple and Cl^- ions in green. The ionic clusters are highlighted by black circles.

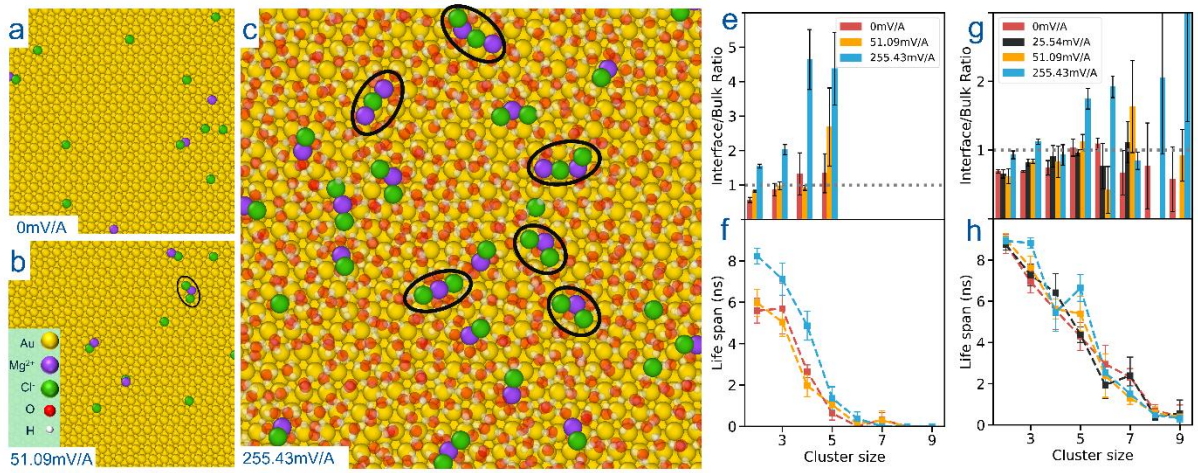

Fig. S19. Simulation results for the 0.71 M $MgCl_2$ solution under various electric potentials. Simulation snapshots of the interface (defined here as the 7 Å from the gold surface) with (a) 0 mV/A, (b) 51.09 mV/A, and (c) 255.43 mV/A. Ionic clusters are shown with black circles. (e) The interface/bulk concentration ratio for clusters formed in the interface to the bulk for 0.71M $MgCl_2$ solution showing an increase for all the cluster sizes illustrating that the cluster formation is enhanced in the interface. (f) The life span of clusters formed in the interface shows that higher voltage leads to the formation of more stable clusters in the cluster size range studied here. For comparison, the same data as (e) and (f) is given in (g) and (h) for the 2.85 M $MgCl_2$ solution. Larger clusters form stably in the higher ionic concentration, but the voltage-induced extension of the cluster's life span is less obvious (although still visible for clusters made of 3 and 5). This is because 2.85 M $MgCl_2$ representing 50% of the salt saturation concentration, more clusters form naturally also in the bulk, making statistics less clear for intermediate voltages/durations.

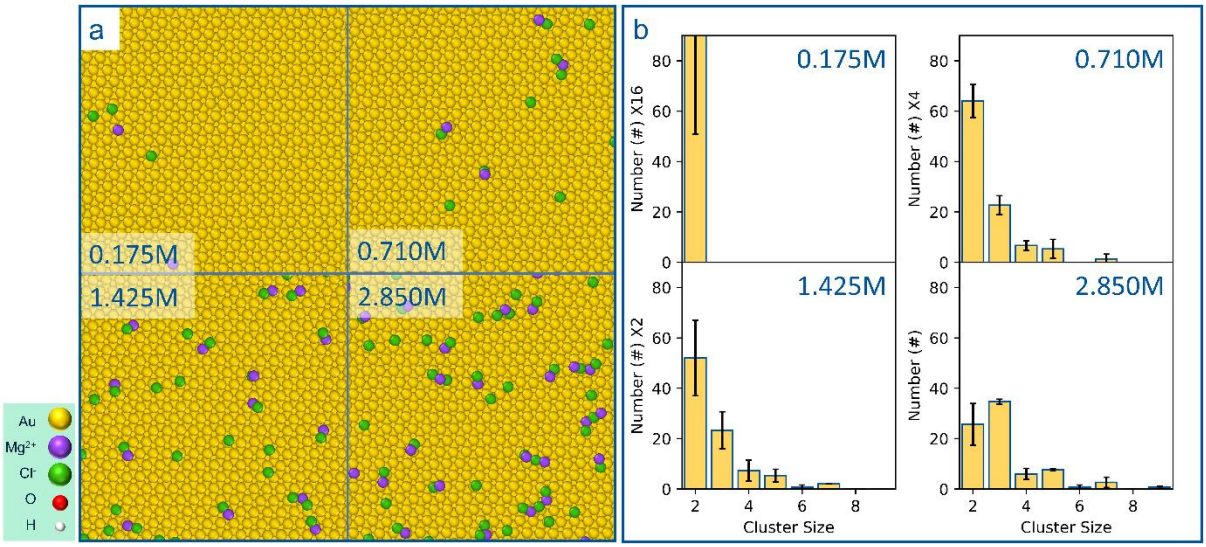

Fig. S20. Simulation results for the $MgCl_2$ solutions with various ionic concentrations under a 51.09 mV/A electric field. Interfacial ionic clusters can form at concentrations lower than 2.85 M . The simulation snapshots (a) of the interface defined as the 7 Å distance from the gold plate for various solutions. (b) The number of clusters with various sizes in the interface and the bulk showing the cluster formation at lower ionic concentrations showing requirement of minimum ionic concentration for cluster formation. The cluster numbers have been scaled according to the ratio of the bulk concentration to the bulk concentration of 2.85 M $MgCl_2$ solution.

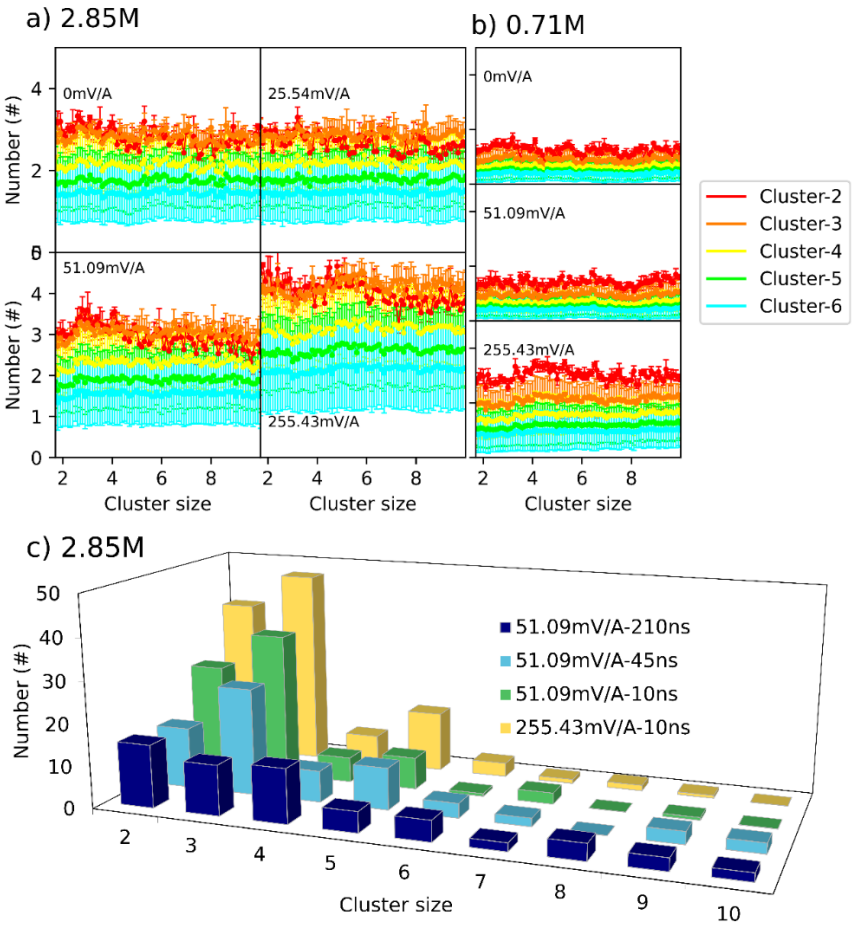

Fig. S21. Time evolution of the number of clusters with various sizes formed in the 5.5 Å interface. The clusters are stable for (a) 2.85 M and (b) 0.71 M solutions of $MgCl_2$ under various external fields. (c) The time evolution of the clusters formed in the interface suggests that even for the lower voltage of 51.09 mV/A larger clusters made of 9 and 10 ions can form in the expense of lower number of smaller clusters (210 ns vs. 10 ns). For longer simulations even the formation of clusters as larger as 20 ions was observed. This is consistent with the idea of nucleation and growth of ionic clusters at the interface. Longer simulation runs are however costly and the associated statistics are limited.

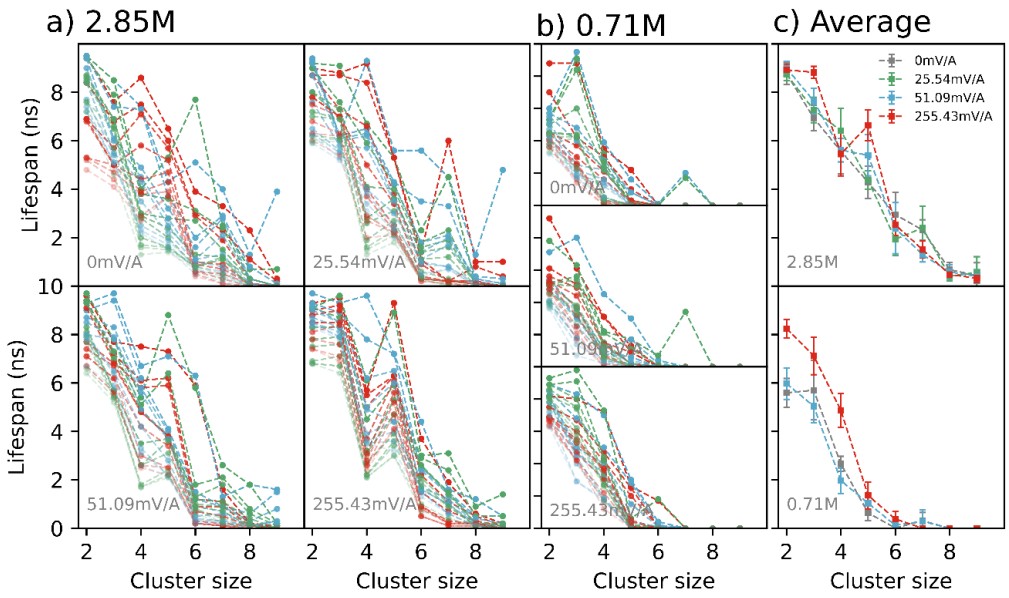

Fig. S22. Statistic of the lifespan of interfacial ionic clusters as a function of ionic concentration. Data from three simulations with a different seed number are shown in each panel (three base colors). For each simulation the lifespans of ten clusters with longest lifespan are shown with different shades of the base color. Lifespans of clusters formed in (a) 2.85 M and (b) 0.71 M $MgCl_2$ solution under different electric fields show an increase in the cluster life with increasing the electric field. (c) Average lifespan for four clusters with highest lifespan. At 0.71 M, increasing the field from 0 mV/A to 255.43 mV/A leads to an increase in the lifespan of all the cluster sizes while at the higher ionic concentration of 2.85 M the lifespan of clusters made of 3 and 5 ions increases with the similar increase in the electric field.

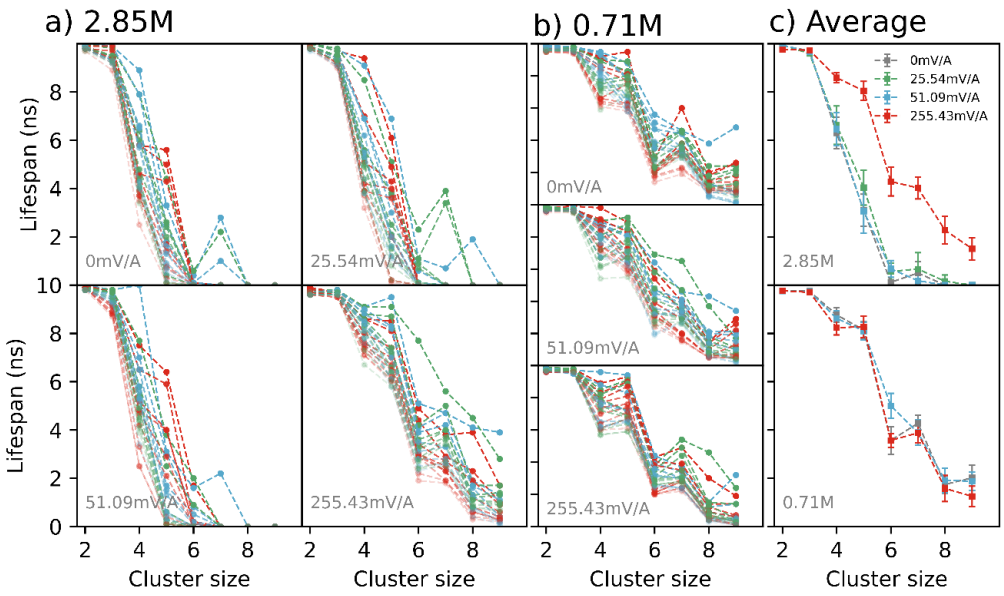

Fig. S23. Statistics of the lifespan of clusters formed in the bulk of the $MgCl_2$ solution, between gold plates. Data from three simulations with a different seed number are shown in each panel (three base colors). For each simulation the lifespans of ten clusters with longest lifespan are shown with different shades of the base color. (a) Clusters in the 2.85 M $MgCl_2$ solution show an increase in lifespan under electric fields. (b) Lifespans of clusters formed in the of 0.71 M $MgCl_2$ shows no effect of electric field on the lifespan of the clusters. (c) Average lifespan for four clusters with longest life.

References

(1) Wu, Y.; Tepper, H. L.; Voth, G. A. Flexible Simple Point-Charge Water Model with Improved Liquid-State Properties. *J. Chem. Phys.* **2006**, *124* (2). https://doi.org/10.1063/1.2136877.

(2) Heinz, H.; Lin, T. J.; Kishore Mishra, R.; Emami, F. S. Thermodynamically Consistent Force Fields for the Assembly of Inorganic, Organic, and Biological Nanostructures: The INTERFACE Force Field. *Langmuir* **2013**, *29* (6), 1754–1765. https://doi.org/10.1021/la3038846.

(3) Hockney, R. W.; Eastwood, J. W. The Particle-Mesh Force Calculation. In *Computer Simulation Using Particles*; CRC Press, 1988; pp 120–165.

(4) Tavakol, M. ClusterAnalysis4WignerCrystals https://github.com/MahdiTavakol/ClusterAnalysis4WignerCrystals/.

(5) Marin-Laflèche, A.; Haefele, M.; Scalfi, L.; Coretti, A.; Dufils, T.; Jeanmairet, G.; Reed, S.; Serva, A.; Berthin, R.; Bacon, C.; Bonella, S.; Rotenberg, B.; Madden, P.; Salanne, M. MetalWalls: A Classical Molecular Dynamics Software Dedicated to the Simulation of Electrochemical Systems. *J. Open Source Softw.* **2020**, *5* (53), 2373. https://doi.org/10.21105/joss.02373.

(6) Serva, A.; Scalfi, L.; Rotenberg, B.; Salanne, M. Effect of the Metallicity on the Capacitance of Gold-Aqueous Sodium Chloride Interfaces. *J. Chem. Phys.* **2021**, *155* (4), 44703. https://doi.org/10.1063/5.0060316.

(7) McDonald, S.; Elbourne, A.; Warr, G. G.; Atkin, R. Metal Ion Adsorption at the Ionic Liquid-Mica Interface. *Nanoscale* **2016**, *8* (2), 906–914. https://doi.org/10.1039/c5nr05833c.

(8) Elbourne, A.; McDonald, S.; Voïchovsky, K.; Endres, F.; Warr, G. G.; Atkin, R.

Nanostructure of the Ionic Liquid-Graphite Stern Layer. *ACS Nano* **2015**, *9* (7), 7608–7620. https://doi.org/10.1021/acsnano.5b02921.

(9) Ricci, M.; Spijker, P.; Stellacci, F.; Molinari, J. F.; Voïtchovsky, K. Direct Visualization of Single Ions in the Stern Layer of Calcite. *Langmuir* **2013**, *29* (7), 2207–2216. https://doi.org/10.1021/la3044736.

(10) Ricci, M.; Spijker, P.; Voïtchovsky, K. Water-Induced Correlation between Single Ions Imaged at the Solid-Liquid Interface. *Nat. Commun.* **2014**, *5* (1), 1–8. https://doi.org/10.1038/ncomms5400.

(11) Gómez Carlos J., C. J.; Garcia, R. Determination and Simulation of Nanoscale Energy Dissipation Processes in Amplitude Modulation AFM. *Ultramicroscopy* **2010**, *110* (6), 626–633. https://doi.org/10.1016/j.ultramic.2010.02.023.

(12) Shannon, R. D. Revised Effective Ionic Radii and Systematic Studies of Interatomic Distances in Halides and Chalcogenides. *Acta Crystallogr. Sect. A* **1976**, *32* (5), 751–767. https://doi.org/10.1107/S0567739476001551.

(13) Nightingale, E. R. Phenomenological Theory of Ion Solvation. Effective Radii of Hydrated Ions. *J. Phys. Chem.* **1959**, *63* (9), 1381–1387. https://doi.org/10.1021/j150579a011.

(14) Loh, S.-H.; Jarvis, S. P. Visualization of Ion Distribution at the Mica−Electrolyte Interface. *Langmuir* **2010**, *26* (12), 9176–9178. https://doi.org/10.1021/la1011378.

(15) Goloub, T. P.; Koopal, L. K.; Bijsterbosch, B. H.; Sidorova, M. P. Adsorption of Cationic Surfactants on Silica. Surface Charge Effects. *Langmuir* **1996**, *12* (13), 3188–3194. https://doi.org/10.1021/la9505475.

(16) Shaw, D. J. *Introduction to Colloid and Surface Chemistry*, 4th ed.; Butterworth-Heinemann, 1992.

(17) Rindelaub, J. D.; Craig, R. L.; Nandy, L.; Bondy, A. L.; Dutcher, C. S.; Shepson, P. B.; Ault, A. P. Direct Measurement of PH in Individual Particles via Raman Microspectroscopy and Variation in Acidity with Relative Humidity. *J. Phys. Chem. A* **2016**, *120* (6), 911–917. https://doi.org/10.1021/acs.jpca.5b12699.